



# Energy absorption of PLA-based metamaterials manufactured by material extrusion: dynamic loads and shape recovery

Maria Pia Desole<sup>1</sup> · Annamaria Gisario<sup>1</sup> · Massimiliano Barletta<sup>2</sup>

Received: 25 October 2023 / Accepted: 9 March 2024 / Published online: 23 March 2024  
© The Author(s) 2024

## Abstract

The objective of the study is to evaluate the performance of solid cellular structures in Poly(lactic Acid) (PLA) by extrusion of material. The structures studied are Strut-Based, Triply Periodic Minimal Surfaces (TPMS) and Spinoidal. Impact tests allowed the identification of three categories of energy absorption (low, medium, high). The structures with lower deformation were subsequently subjected to cyclic impact tests, while the others were discarded from the analysis. Once the structures were deformed, they were immersed in a thermostat bath at 70 °C, a temperature higher than the glass transition of PLA, necessary for the recovery of shape. TPMS structures display the best performance for high and medium impact energies, thanks to the presence of few internal defects. Spinoidal structures perform well at low impact energies but are less suitable for cyclic testing due to their geometric characteristics. Despite featuring the same density of TPMS structures, the strut based ones are not suitable for cyclic testing due to poor mechanical strength. The experimental findings are very promising as the best performing structures can be suitable for the fabrication of products with an increased life cycle, especially in the ever growing and flourishing market of technical items for impacts protection.

**Keywords** 4D Printing · Metamaterials · Material Extrusion · Shape Memory Materials · Energy Absorption

## 1 Introduction

4D printing is one of the most innovative technologies of recent years. Its origin dates back to 2013 thanks to the studies conducted by the research group of MIT (Massachusetts Institute of Technology) [74]. These studies are based on 3D printers, an additive manufacturing technology that has allowed greater precision in the production of end-goods [56], through a layer-by-layer manufacturing process that allows the manufacture of three-dimensional objects [38, 82]. 4D printing represents, in particular, an evolution of 3D printing, as the functionality, properties and shape of the product can also vary as a function of time [55], which becomes the fourth dimensional variable of the

manufacturing process [10, 17]. Furthermore, 4D printing allow to confer functions such as self-assembly, multi-functionality and self-repair [46].

In the context of 4D printing, the development of Shape Memory Materials (SMM) is of utmost interest. SMM are materials capable of recovering the original shape after a permanent deformation, once subjected to an external stimulus [22]. These materials can be activated by different types of stimuli, such as thermal ones [37, 68, 75], mechanical [23, 29, 47], luminous [24, 30], electrical [14, 60], magnetic [44, 64] or chemical [32, 90], exploiting the material shape memory effect (SME) [80, 91]. In particular, shape memory polymers (SMPs), once permanently deformed, are fixed in their provisional temporary configuration [31]. They therefore have the ability to recover their permanent shape when heated to a temperature higher than the glass transition temperature of the material [89].

Metamaterials are artificial materials characterized by an engineered architecture. They can exploit the shape recovery capabilities of SMMs. They are designed in order to have physical properties determined by the geometry of the “cellular” structure rather than the chemical composition of the material [48, 83]. Furthermore, these materials

✉ Massimiliano Barletta  
massimiliano.barletta@uniroma3.it

<sup>1</sup> Dipartimento Di Ingegneria Meccanica E Aerospaziale, Sapienza Università Di Roma, Via Eudossiana 18, 00184 Rome, Italia

<sup>2</sup> Dipartimento Di Ingegneria Industriale Elettronica E Meccanica, Università Degli Studi Roma Tre, Via Vito Volterra 62, 00146 Rome, Italia

have unique characteristics not found in other types of material, such as, for example, low density [71], high stiffness and mechanical strength [63, 76] as well as negative Poisson's ratio [6, 8].

Numerous studies [16, 35, 45, 85] have attributed to metamaterials excellent energy absorption capabilities both for metallic [70, 88] and polymeric [1, 69] materials.

Poly(lactic acid) is widely used among thermoplastic polymers in additive technology and the design of cellular structures. [13] analyzed sandwich structures made of FDM with fragile core with high mechanical strength in PLA, instead of fossil-based plastics such as poly(vinyl chloride) and poly(ethylene terephthalate). PLA is the base material and it is inserted in between two unidirectional glass fiber reinforced polymer by compression molding so as to form a sandwich structure. This configuration improves the mechanical properties of the sandwich structure, both in terms of shear strength, Young's modulus and bending load. In another study [11] studied sandwich structures in continuous fibre reinforced PLA together with sandwich composites containing short polyester fibre and PLA. The extrusion of the material took place in a vacuum glass chamber, with the analysis considering three types of surface coatings. The use of flax fibre demonstrated a similar durability with respect to conventional glass fibre composites. In addition, the presence of the microsilice/epoxy resin coating improved the mechanical and stability properties of the structures. Finally, [12] studied thermoplastic matrix composites reinforced with carbon fiber acting as heating element. This design led to a significant improvement in thermal resistance, especially at the edges of the heating element. The choice of the geometry of the structure is a fundamental step, as it affects the performance and properties of the material itself. Recently, the Triply Periodical Minimal Surfaces (TPMS) structures have attracted considerable attention. TPMS are geometries that repeat themselves in three dimensions with zero mean curvatures and large surface areas [39]. In [57], the TPMS structures in 316L steel manufactured using LPBF (Laser Powder Bed Fusion) were tested in compression. They highlighted how the Nevious structure is the best in absorbing energy up to strain equal to 50%. In terms of elastic modulus, the best geometries were found to be the Fischer Koch with 6.96 GPa, the Nevious with 6.74 GPa and the Gyroid 4.46 GPa. The Diamond, Nevious and Gyroid geometry showed higher yield strength with values ranging between 71–83 MPa. [36] studied the mechanical behavior of different TPMS such as the Primitive and Gyroid structures fabricated by SLM (Selective Laser Melting). The Gyroidal structure was found to gradually deform during compression and show highly hardened areas, due to the presence of macro-localities where the geometry underwent high deformations. The Primitive structure instead showed a rapid local deformation after the application of the static load, but it exhibited

a better capacity to absorb energy in case of structures with relative densities  $< 0.35$ .

TPMS are studied as energy absorbers, when made with metallic materials. However, the existing literature lacks information regarding TPMS structures fabricated with polymeric materials. Biopolymers such as PLA (polylactic acid) represent an excellent alternative to conventional shape memory polymers, as in addition to having good mechanical resistance, they are environmentally sustainable (Caceres-Mendoza et al., 2023).

Strut-based structures are often used in metamaterial applications. These are reticular structures made up of unit cells that repeat themselves on a regular and periodic basis. In [72], the BCC (Body-Centered Cubic) lattice was found to boast good energy absorption for relative densities of 10, 20 and 30%, respectively, but still lower than those of the FCC (Face-Centered Cubic) of equal density. Furthermore, once stressed in compression, the response at break of the BCC lattice is stable and remains so until the densification condition. [86] compared the performance in terms of energy absorption of the TPMS structures with the BCC structures, highlighting how the former are superior, even in terms of fluctuation of the stress level in the plateau region, i.e. in the area of the stress–strain curve in which the load is almost constant [20]. Another category of structure that could guarantee good absorption capacity and mechanical resistance is the Spinoidal. This structure consists of smooth and non-intersecting surfaces with almost zero mean curvature [27, 66]. In the scientific literature, the behaviour of Spinoides is not investigated, with the exception of some studies where their behaviour as acoustic absorbers is analysed [79].

More in detail, the mechanical properties of metamaterials and their ability to absorb energy are extensively studied mainly under compressive stresses [7, 36, 42, 50, 62, 77]. Much less frequent is the study of energy absorption when dynamic loads are applied to the structures [25, 52]. In these studies, however, the number of geometries investigated is limited. Furthermore, there is a lack of specific assessments in which the resistance of the structure in withstanding load cycles is also associated with the subsequent recovery phase. Recently, [18] have addressed these issues with reference to chiral geometries that are tested under compression load. The resistance to cyclic stress would ensure prolonged use of the product and would allow for a reduction in the weight of the component, thanks to the adoption of low-density grids or patterns. The number of cycles applicable to the structure is strictly dependent on the lattice geometry analysed and on the characteristics of the chosen material. In this context, the aim of the present work is to investigate the mechanical performance provided by Strut-based, TPMS and Spinoidal metamaterial structures made of PLA, once subjected to dynamic loads applied by a machine designed to perform impact tests. Initially, the strength of structures for various

impact energies was tested. Three ranges have been defined for the impact energy: high, medium and low. Once the best geometries for each category had been identified, i.e. those which did not show a plastic deformation such as to prevent further impact tests, the structures were restored to their original form by applying a thermal stimulus transmitted via a thermostatic bath. The structures have therefore been subjected to a sequence of cycles of stress—recovery of shape, to evaluate their energy absorption capacity. The structures chosen for each category were compared by identifying a correlation between mechanical properties as the absorption energy and the ability to recover the shape, a typical effect of SMPs. The best geometries for high and medium impact energies were found to be the TPMS, as the limited internal manufacturing defects do not compromise the mechanical resistance of the structure, nor the shape recovery. For low impact energies, on the other hand, the Spinoidal structures showed better behaviour even in the case of cyclic stress. Finally, a relationship between damage status and speed of recovery of the different structures investigated was identified. A more damaged structure recovers its shape in less time, except for the lamellar Spinoidal structure as it features a lower stiffness. The Spinoidal structures, instead, when subjected to cyclic stresses, deforms plastically, compacting in such a way and increasing their overall strength as to be unable to recover the initial height.

## 2 Materials and methods

### 2.1 Materials

For the manufacturing of the samples, a PLA filament (Ulti-maker, Utrecht, Netherlands) was used. The choice to use technical PLA was determined by the need to obtain greater mechanical resistance than that which would be obtained using non-technical PLA filaments. Furthermore, the technical filament showed less brittleness than standard PLA

[53]. The diameter of the filament is  $2.85 \pm 0.10$  mm, with a density of  $1.22 \text{ g/cm}^3$ .

### 2.2 Geometry definition and design

The analysed structures are three-dimensional of the non-stochastic type, characterized by a unitary lattice cell repeated within the volumetric region [5, 54], with the exception of the Spinoides which instead are stochastic structures [26, 78]. In this study, three types of patterns were designed: Strut-based, TPMS and Spinoidal. For the first two categories of cellular structures, the pattern density was set at 30%, a value below which it is possible to define a structure as cellular [15]. The relative density of the Spinoidal structures was set at 0.50, as problems in the fabrication were encountered for lower values. The dimensions of the samples are  $30 \times 30 \times 30 \text{ mm}^3$  with the insertion of a 0.5 mm thick bottom layer to allow the correct gripping of the sample on the machine during the manufacturing process.

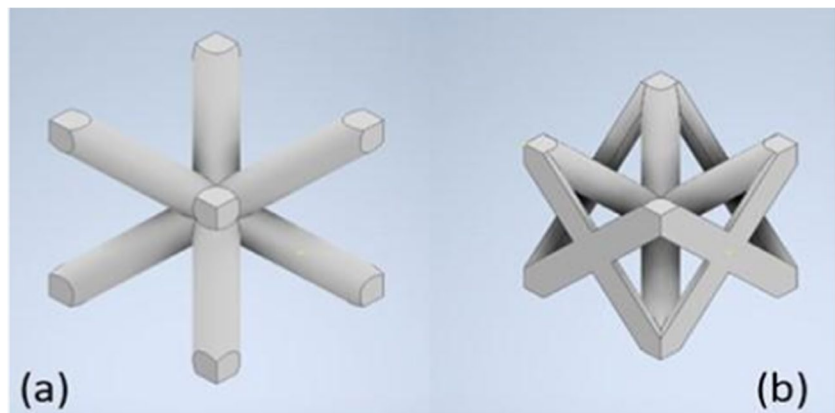
#### 2.2.1 Strut-based structures

The Strut-based structures investigated are essentially two: BCC (Body Centered Cubic) and FBCC (Face Body Centered Cubic) already analysed in [19, 34, 40]. The structures were created using the "Autodesk Inventor 2022" software, considering the size of the single cell equal to  $6 \times 6 \times 6 \text{ mm}^3$ . The diameter of the single rod that makes up the BCC structure was calculated as explained in [9], setting the length of the 4 beams of the cell (Fig. 1a) to 10.392 mm. The volume of the single cell and the relative density of the structure can be calculated as in Eqs. 1 and 2:

$$V_{\text{cella BCC}} = 4(\pi r_{\text{BCC}}^2)h = \pi D_{\text{FBCC}}^2 h \quad (1)$$

$$\rho = \frac{\text{Volume occupato}}{\text{Volume totale}} = \frac{V_{\text{cella BCC}}}{V_{\text{CUBE}}} \quad (2)$$

**Fig. 1** **a** BCC cell CAD model, **b** FBCC cell CAD model



Having imposed the height of the cell at 6 mm, the volume of the entire cube in which the cell is inscribed is equal to  $V_{CUBE} = (6\text{mm})^3 = 216\text{mm}^3$  and imposing the density equal to  $\rho = 0.30$ , the diameter of the single rod will result according to Eq. 3:

$$D_{BCC} = \sqrt{\frac{V_{CUBO} * \rho}{V_{cella BCC} * \pi}} = \sqrt{\frac{216\text{mm}^3 * 0.3}{2 * 10.392\text{mm} * 3.14}} \approx 1.4\text{mm} \quad (3)$$

In a similar way it is possible to measure the diameter of the rod for the FBCC cell (Fig. 1b). In this second case, there is a greater quantity of material due to the addition of the semi-beam on the external faces. For this reason, the volume of the FBCC can be defined as equal to twice the volume of the BCC, which according to Eq. 4 will be equal to:

$$V_{cella FBCC} = 2V_{cella BCC} = 8(\pi r_{FBCC}^2)h = 2\pi D_{FBCC}^2 h \quad (4)$$

Considering the relative density of the structure equal to 30% and  $V_{CUBE} = 216\text{mm}^3$ , the diameter of the beam for the FBCC structure can be calculated according to Eq. 5:

$$D_{FBCC} = \sqrt{\frac{V_{CUBO} * \rho}{V_{cella FBCC} * \pi}} = \sqrt{\frac{V_{CUBO} * \rho}{V_{cella FBCC} * \pi}} \approx 0.99\text{mm} \quad (5)$$

### 2.2.2 TPMS Surface-based structures

The Triply Period Minimal Surface (TPMS) are structures that are characterized by surfaces with zero mean curvature [49, 84]. The geometries were generated starting from the Matlab MS lattice application [3]. The structures shown in Fig. 2 are:

(a) Diamonds:

$$F(x, y, z) = \sin \sin (x) * \sin \sin (y) * \sin \sin (z) + \sin \sin (x) * \cos \cos (y) * \cos \cos (z) + \cos \cos (x) * \sin \sin (y) * \cos \cos (z) + \cos \cos (x) * \cos \cos (y) * \cos (z) \quad (6)$$

(b) Fischer-Koch:

$$F(x, y, z) = \cos \cos (2x) * \sin \sin (y) * \cos \cos (z) + \cos \cos (x) * \cos \cos (2y) * \sin \sin (z) + \sin \sin (x) * \cos \cos (y) * \cos (2z) \quad (7)$$

(c) FRD:

$$F(x, y, z) = (x) * \cos \cos (y) * \cos \cos (z) - [(2x) * \cos \cos (2y) + \cos \cos (2y) * \cos \cos (2z) + \cos \cos (2z) * \cos (2x)] \quad (8)$$

(d) Gyroids:

$$F(x, y, z) = \cos \cos (x) * \sin \sin (y) + \cos \cos (y) * \sin \sin (z) + \cos \cos (z) * \sin \sin (x) \quad (9)$$

(e) IWP:

$$F(x, y, z) = (x) * \cos \cos (y) + \cos \cos (y) * \cos \cos (z) + \cos \cos (z) * \cos (y) - (2x) + \cos \cos (2y) + \cos \cos (2z) \quad (10)$$

(f) Nevious:

$$F(x, y, z) = (x) + \cos \cos (y) + \cos \cos (z) + 4 * (x) + \cos \cos (y) + \cos \cos (z) \quad (11)$$

(g) PMY extension

$$F(x, y, z) = 2 * \cos (x) \cos (y) \cos (z) + \sin (2x) \sin (y) + \sin (x) \sin (2z) + \sin (2y) \sin (z) \quad (12)$$

(h) Primitives:

$$F(x, y, z) = \cos \cos (x) + \cos \cos (y) + \cos \cos (z) \quad (13)$$

In Eqs. (6, 7, 8, 9, 10, 11, 12, and 13) the mathematical functions of the various geometries are reported [33, 73] and [59]. Table 1 shows the parameters used to generate the geometry through the application. After inserting the inputs, a geometry file in \*.stl format is obtained.

### 2.2.3 Spinoidal structures

The geometries shown in Fig. 3 are Spinoidal, respectively columnar (a), cubic (b), isotropic (c) and lamellar (d).

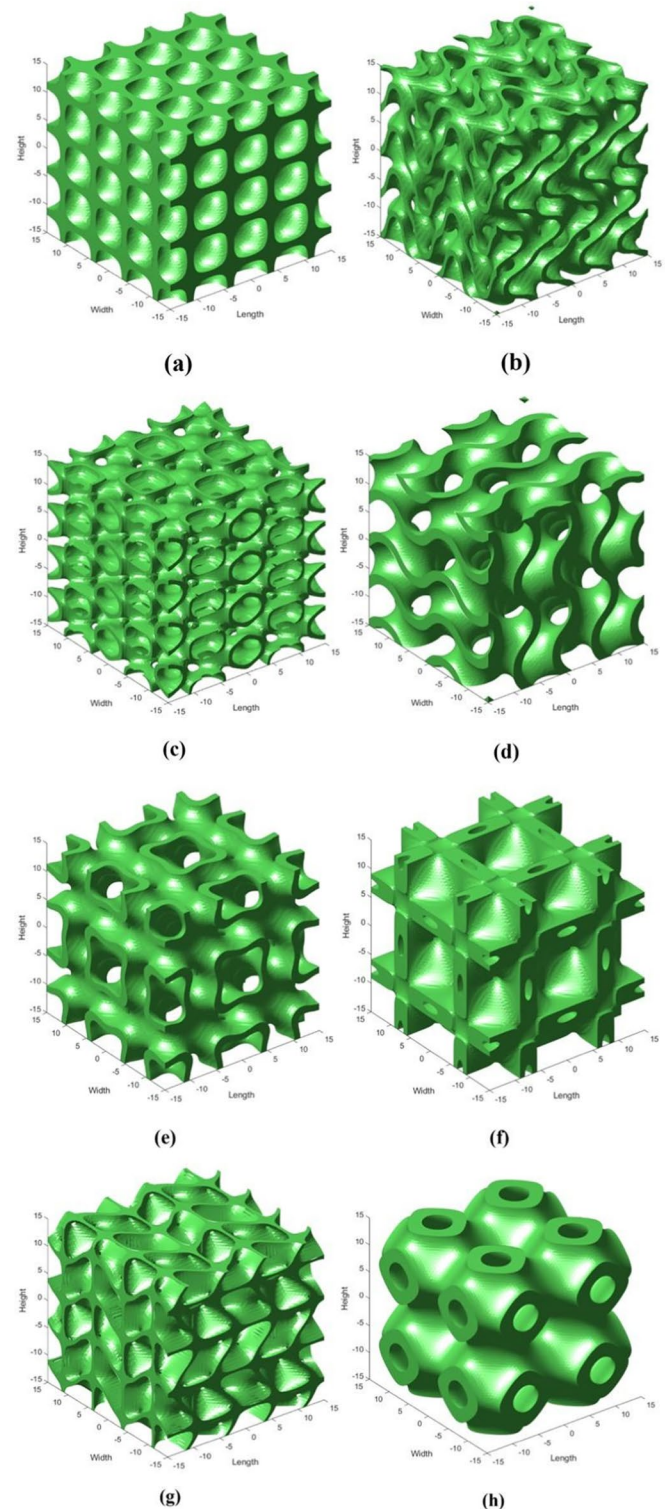
The geometries were created by the Matlab software using the codes made available by the Gibbon tool [43]. To generate these structures, a random field of radial Gaussian functions (GRFs) was used. The size of the domain, where the GRF function was sampled, was set to 1. The sampling resolution was set to 100. Next, the wavenumber and wavenumber for the function GRF were set to  $15\pi$  and 1000, respectively. After calculating the solid geometry and creating the corresponding mesh, the model was exported to a file in a \*.stl format.

## 2.3 Geometry manufacturing with FDM technology

The specimens were produced using the “Ultimaker S5” 3D printer (Ultimaker, Utrecht, Netherlands). For the Strut-based structures it was necessary to convert the \*.ipt format CAD files into a \*.stl format files. While for the TPMS and Spinoidal structures this step was not necessary, as a



**Fig. 2** TPMS structures: Dia-  
mond (a) Fischer-Koch (b) FRD  
(c) Gyroid (d) IWP (e) Nevious  
(f) PMY (g) and Primitive (h)



file of this type is already obtained in output to the generation code. The printing temperature was set at 215 °C, the height of the layer which was instead assumed to be equal to 0.2 mm. The printing speed was set to 60 mm/s in order not to induce residual tensions within the material [87]. Furthermore, a filling density of 100% was set

to maximize the mechanical resistance [58]. The printing bed temperature was set at 60 °C to ensure sufficient bond strength during the printing process [67]. The structures investigated do not have thin elements in contact with the hot plate. Therefore, it was not necessary to insert a water-soluble polymer support during the manufacturing process.

**Table 1** Inputs required for geometry generation entered into the MS Latex application

Geometry generation input	
Relative densities (%)	30
Unit cell size (mm)	15
Sample length (mm)	30
Sample Width (mm)	30
Sample Height (mm)	30
Mesh density point	40

## 2.4 Impact test

The impact tests were carried out using a custom-built machine which involved the fall of a 6.5 kg steel weight from an adjustable height (i.e., maximum height of 0.9 m). The experimental results were considered for comparative

purposes as the same architecture of the tests was kept during the experimental plan.

Figure 4 shows the frame of the machine used. The sizing of the machine was determined considering a maximum impact energy imposed on the specimens of approximately 58 J [4, 61, 87].

The grave was chosen in steel, therefore the density is known  $\rho = 7810 \frac{\text{kg}}{\text{m}^3}$ . A diameter of 5.8 cm was set. The grave is bound by the presence of the plexiglass tube which guides its motion during the test. The mass of the grave, once the height  $h_{\text{grave}} = 0.3$  m has been set, can be expressed by Eq. (14):

$$m_{\text{grave}} = \rho * V_{\text{grave}} = \rho * \left[ \left( \frac{\pi d_{\text{grave}}^2}{4} \right) * h_{\text{grave}} \right] = 6.5 \text{Kg} \quad (14)$$

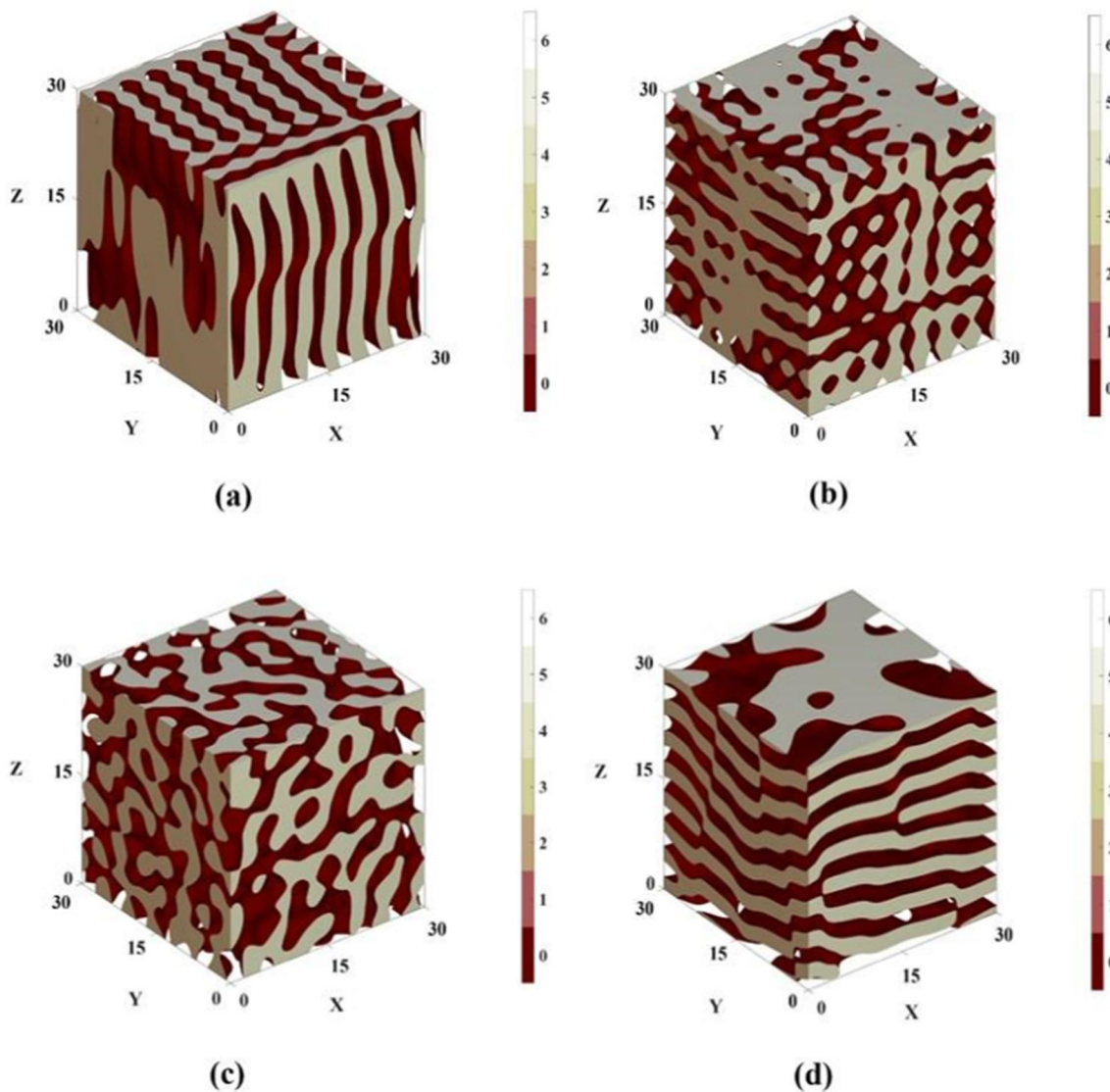


**Fig. 3** Spinoidal structures: Columnar (a) Cubic (b) Isotropic (c) and Lamellar (d)

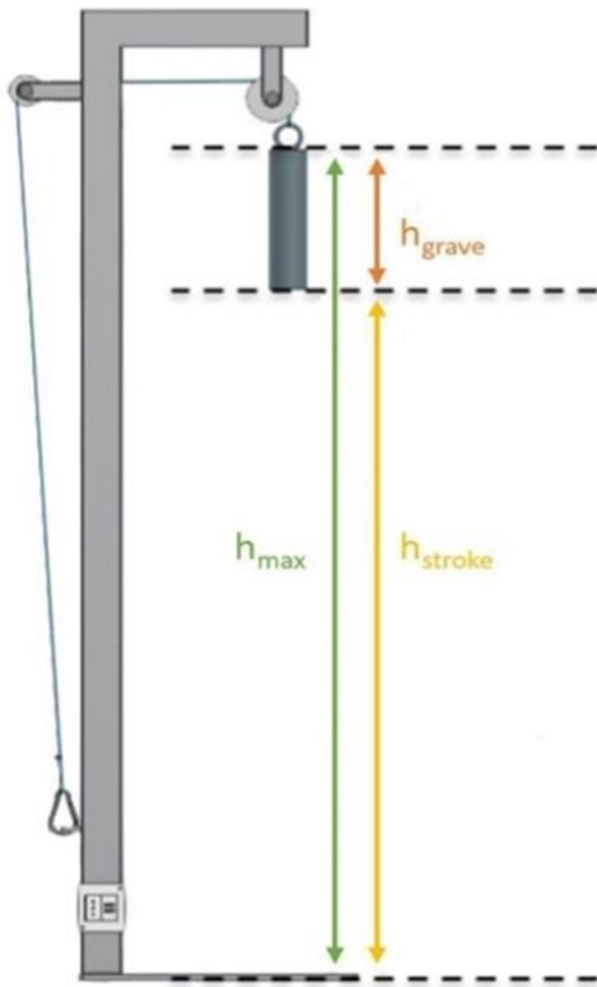


**Fig. 4** Frame of the machine with which the impact tests are conducted

The only unknown is  $h_{stroke}$ , i.e. the maximum impact height that can be set, which can be calculated using Eq. (15), imposing  $g = 9.81 \text{ m/s}^2$  and the principle of conservation of mechanical energy

$$m_{grave} * g * h_{stroke} = \frac{1}{2} * m_{grave} * v^2 \cong 57.4J \tag{15}$$

As  $h_{stroke}$  is equal to 0.9 m, it is possible to determine the height  $h_{max}$  which includes both the height of the grave and the maximum impact height. This height is fixed at 1.2 m, which is suitable to avoid an excessively tall structure.

Table 2 shows the correspondence between the falling height of the body and the associated impact energy. The energy range referred to is between a maximum of 57.4 J, obtained when the object is dropped from the maximum height of 0.9 m to a minimum of 19.1 J, when the object is dropped from the minimum height, i.e. 0.1 m.

**Table 2** Correspondence between severe fall height and impact energy

Severe fall height (m)	Impact energy rating (J)
0.9	57.4
0.8	51.8
0.6	38.3
0.5	31.9
0.4	25.5
0.3	19.1
0.2	12.7
0.15	9.6
0.1	6.4

In an initial phase, the strength at break of the different structures was tested by setting the maximum height and energy level. To determine a level of impact height and energy that would not cause permanent deformations on the specimens, the structures involved were subjected to tests at progressively lower heights. This process allowed to define a combination of impact height and energy that would preserve the integrity of the specimen. Such combination should allow the specimen to be restored to the initial shape for any load and recovery cycles, allowing it to be retested in the subsequent steps of the investigation.

For each type of structure, three replicas were tested to obtain an accurate and representative evaluation of the results. During the tests, the pre- and post-impact height of the samples is measured. However, the measurements are influenced by the high variability of the geometry in the upper part of the sample, where a proper smooth top layer is not present. Thus, measuring the samples with the calliper becomes very complex and inaccurate. To solve this problem, flat plates larger than the base of the cube were interposed between the movable and fixed beaks of the calliper, the CAD model of which is shown in Fig. 5a. The presence of these two elements allowed to measure with good accuracy the distance between the two extremes, i.e. the lower and upper peak as shown in Fig. 5b. The dishes were made of aluminium with a mirror finish.

### 2.5 Shape recovery

After the impact tests, the recovery processes of the shape of the structures are carried out by applying an external thermal stimulus. The stimulus is provided by dipping the samples in a temperature-controlled bath with an immersion thermostat C series (Julabo GmbH Seelbach, Germany), inside

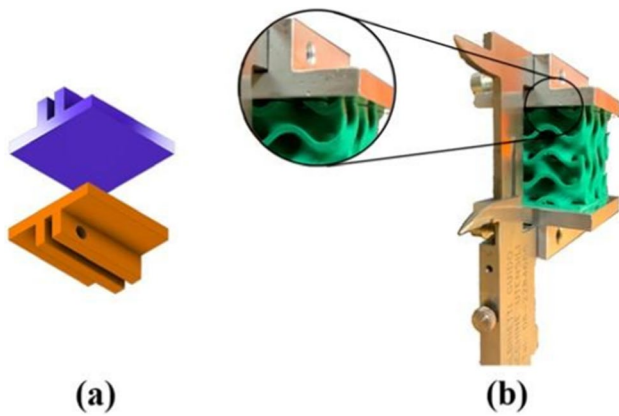


**Fig. 5** **a** CAD model of the measuring plates, **b** Contact between plate and specimen surface

a transparent tank with a capacity of 19 L. The temperature was set at 70 °C, higher than the glass transition temperature of polylactic acid  $T_g = 58$  °C [41].

Tracking software was used to monitor the sample recovery. To prevent the formation of deposits inside the bath, 70% demineralised water and 30% natural water have been used, so as not to compromise the sharpness of the images. The dipping of the specimen inside the bath was carried out using a support consisting of a clamp equipped with a handle to facilitate entry and exit from the tank, as shown in Fig. 6.

The support consists of two parts, a fixed base for supporting the frame and a smaller mobile one for containing the sample during the test, both made of aluminium to withstand high temperatures. The approach between the fixed and the mobile part takes place through the presence of two cylindrical guides and a central pin completely threaded and screwed inside the two parts. To facilitate the approach phase, a knob has been created which rotates the head of the bolt, recalling the mobile part from the fixed one and reducing the distance between the two parts. The knob, the

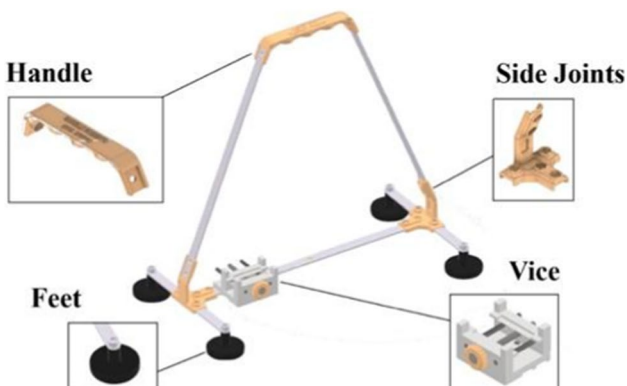


**Fig. 6** Support used for the immersion of the sample in the thermo-static bath

side joints of the clamp and the handle that allows the correct immersion/extraction of the clamp itself in the thermo-static bath are made by SLA (Stereolithography) (Formlabs FORM 3 printer). The photopolymer resin used is able to withstand temperatures of 238 °C, thus avoiding problems of contact with a liquid at high temperatures. The feet of the clamps are made of black plastic material, with a radius of connection identical to that of the internal corners of the tank. This choice allows to place the clamp in the same position, ensuring greater stability and facilitating repeated use. The lower bars of the clamp have a specific length of 30 cm, equal to approximately two thirds of the total length of the tank, further contributing to the safety and efficiency of using the device.

Recordings of the sample shape recovery were made with a full HD video camera (GZ-E205, JVC, Yokohama, Kanagawa, Japan). The tracking software makes it possible to trace a specific pixel and to follow its movements over time, following the definition of a fixed reference system as shown in Fig. 7. In particular, the software provides the possibility of distinguishing the selected pixel among those in the neighbourhood by means of an algorithm which is based on the reiteration in each frame of the method of the occurrence matrices. Furthermore, the system allows the option of selecting a fixed reference measurement, in this case the length of the clamp. This makes it possible to associate a measurement of the distance travelled to the movement of the pixel to be able to calculate the actual distance travelled over time from the point chosen as a reference. The tracking process is facilitated by the presence of a red marker to enhance the contrast between the pixel and the adjacent ones.

## 2.6 Deformation analysis and application of cyclic loads

Once the best structures have been defined for each category, cyclic stressing of the structures was performed. Cyclic tests

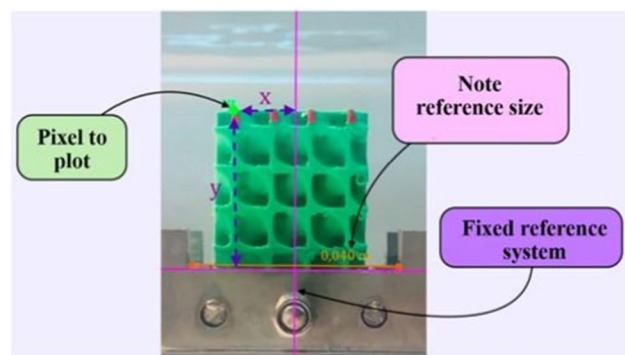


**Fig. 7** Identification of the reference pixel, of the fixed reference system and of the known measurement, for the operation of the tracking software



are carried out by testing the specimens at the heights that corresponds to each macro-category of impact energy. In the case of high impact energies, the selected structures were tested at heights of 0.9 m, 0.8 m and 0.6 m, respectively, that correspond to energies of 57.4 J, 51.8 J and 38.3 J. For an average (medium) impact energy level, the structures are tested at heights of 0.6 m, 0.5 m and 0.4 m. For the lowest impact energies, the heights considered are between 0.3 m and 0.1 m. Subsequently, load-recovery cycles were carried out.

The number of cycles investigated are variable, being based on the specific mechanical properties of the structure studied. The tests on the individual structures were carried out in a single day to have sufficiently reliable results and to avoid the effects of the aging process of the material.

### 3 Results

#### 3.1 Identification of impact resistance categories

In the first part of the experimental investigation, the specimens are tested up to break by identifying the corresponding impact heights and maximum energies. Subsequently, the samples that have been broken are tested with impacts heights and energy progressively lower to measure the deformation achieved. This procedure allowed to identify three categories of impact resistance for all the investigated structure, as it is defined in Table 3. Each structure tested is therefore classified within a specific category: high, average, low.

As earlier mentioned, the definition of the impact categories was based on the identification for a threshold value both in terms of the falling height of the body during the impact test and the resulting impact energy. The defined value allows the structures to deform mostly in the elastic range, bringing back to the smallest plastic deformations following the impact itself. This in turn creates the conditions for a possible subsequent recovery of shape and the possibility of submitting the structures to repeated cyclic stresses, as it happens in the second part of the experimental investigation.

The category characterized by the lowest impact energy (namely, Low) requires a greater number of experimental levels during the impact tests to avoid that some structures are broken whatever the energy value is set, while others only undergo deformations in the elastic range. In this way, a correct balance can be achieved between the capacity of each sample to absorb the impact energy and the possibility of a subsequent recovery of shape. This would allow to study under cyclic stress the structure of interest.

Figure 8 illustrates the trend of the height variation  $\Delta l$  of the specimens, which represents the difference in height respectively of the specimen after the manufacturing by 3D

**Table 3** Impact resistance categories with the corresponding heights and impact energies

CATEGORY	HEIGHTS (m)	ENERGY (J)
High	0.9	57.4
	0.8	51.8
	0.6	38.3
Medium	0.6	38.3
	0.5	31.9
	0.4	25.5
Low	0.4	25.5
	0.3	19.1
	0.2	12.7
	0.15	9.6
	0.1	6.4

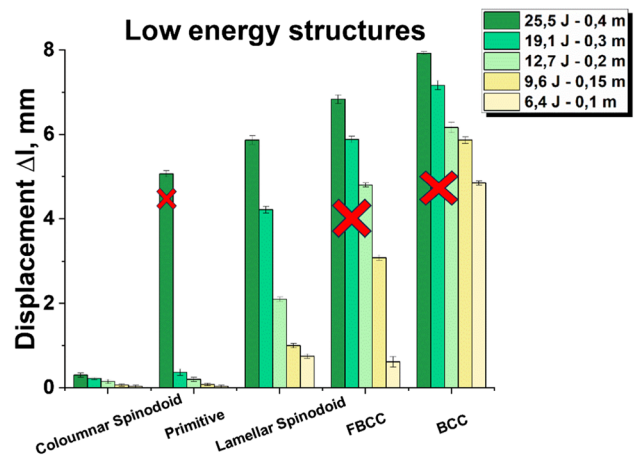


**Fig. 8** Trend of displacement  $\Delta l$  as energy and impact height vary for low energy levels

printing and that after the impact test, precisely after impact tests led at low impact energy.

The histogram highlights the different behaviour between the Columnar and Lamellar Spinoidal structures. In the first case, displacements of less than 1 mm are recorded, for all energy sub-categories. The Lamellar Spinoidal structure, on the other hand, has limited displacements only for impact energies lower than 10 J. However, as the energy increases, the displacement  $\Delta l$  also increases reaching values close to 6 mm. In both cases, the structures have a high capacity to absorb the impact energy in the respective deformation fields, elastic–plastic for the Lamellar and only elastic for

the Columnar structure. The other structures do not prove as effective in resisting the impact. Therefore, they were not tested under cyclic stress, as this kind of test would quickly lead them to collapse.

The Strut-based structures BCC and FBCC broke for impact heights greater than 0.15 m. Therefore, they cannot be tested further under cyclic stress, due to their low impact resistance as well as due to the strong localization of the stresses near the central nodes of the individual cells. Also the Primitive structure cannot be tested further under cyclic stress, as for impact energy around 38 J, the displacement  $\Delta l$  undergoes an increase of 7.2% and the structure is broken.

For the structures tested at medium impact energy (namely, Average), an energy range between 25.5 J and 38.3 J is considered and a corresponding height range between 0.4 m and 0.6 m. Figure 9 shows the histogram of the mean and standard deviation of the displacement  $\Delta l$  measured during the test.

The Diamond Lattice structure shows greater impact resistance, as the displacement  $\Delta l$  is limited compared to other geometries and therefore more suitable to be tested under cyclic stress. In [65], the Diamond structure fabricated from PLA exhibits higher mechanical strength than the Nevius structure and higher energy absorption for strains of 30%. The other structures, all belonging to the surface-based category, show higher deviations and higher deformations once subjected to impact. In particular, for energies of 38.3 J, the Nevius structure shows displacements slightly higher than the Diamond structure, with the displacement  $\Delta l$  upper deviation being 10%. At the same time the structure cannot be tested under cyclic stress. The PMY structures and the FRD cannot be tested under cyclic stress because for impact energies higher than 31.9 J, they show a high plastic deformation, which leads to their irreversible failure.

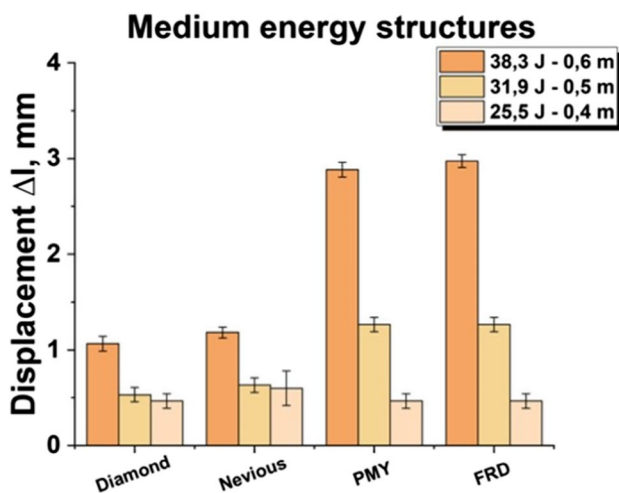


**Fig. 9** Trend of displacement  $\Delta l$  as energy and impact height vary for average energy levels

Consequently, recovering their shape later is useless as they are irreparably damaged by the first impact.

The geometries tested at high impact energies (namely, High) are tested at impact heights which correspond respectively to 38.3 J, 51.8 J and 57.4 J. The structures which are best suited to operate with high impact energy impacts are those which are not irreparably damaged after the first impact and that are virtually insensitive in low and medium energy impact tests. Figure 10 shows the histogram with mean and standard deviation of the displacement  $\Delta l$  measured during the impact tests. The Gyroid structure and the Cubic Spinoidal structure show greater strength. Therefore, they will be analysed later under cyclic stress. Although the Spinoidal structure is the best in terms of displacement  $\Delta l$ , the Gyroid structure was also included in the investigation in order to make a comparison between two different types of structures. In fact, these structures have two different types of filling. The TPMS structure appears, in fact, more regular than the Spinoidal one which is instead more randomized.

Lastly, during the impact tests at average impact energy, the Diamond structure showed a remarkable resistance to deformation. Therefore, it was deemed appropriate to be also tested for high impact energies. The displacements  $\Delta l$  of the Diamond structure are higher than those of the Gyroid structure and the Cubic Spinoidal structure by 52 and 65%, respectively, when considering impact heights of 0.9 m. For impact heights of 0.8 m, the difference is 65 and 80%, respectively. Finally, for impact heights of 0.6 m, there is a difference of 59% with the Gyroidal structure and of 30% with the Spinoidal one. Despite the higher deformations, the Diamond structure was tested under cyclic stress, as the maximum displacement still remains less than 10% of the height of the cubic structure. Accordingly, the Isotropic Spinoidal, IWP and Fischer-Koch structures were not tested under cyclic stress. The structures chosen at the end of the

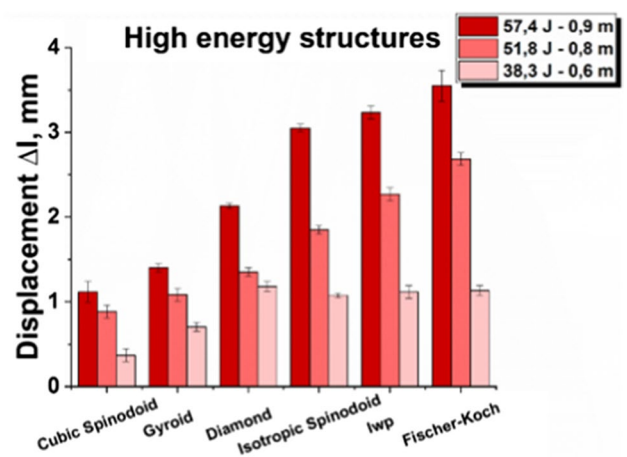


**Fig. 10** Trend of displacement  $\Delta l$  as energy and impact height vary for high energy levels

impact tests for each energy category are, therefore, shown in Fig. 11.

### 3.2 Tests with cyclic load—recovery of shape

#### 3.2.1 Structures with high impact energy

The second step of the experimental investigation was conducted after the selection of the best geometries. During this step, the selected structures are submitted to cyclic loads. The resulting shape is subsequently restored through a heating process. The high impact energy structures tested were submitted to cyclic stresses at heights of 0.6, 0.8 and 0.9 m, in agreement with the values reported in Table 3. Table 4 shows the initial height, the height following the impact and the height recorded after the recovery of the shape, respectively, for impacts at 0.6 m, corresponding to 38.3 J as impact energy. For the Gyroid structure, the initial heights for the first three cycles are lower compared to the height after the shape recovery, highlighting the complete recovery of the height. This phenomenon can be justified by considering two fundamental aspects: (i) the effect of the pressure exerted by the water bath on the structure during the recovery step; (ii) the state of damage of the material [21, 81]. During the cyclic stresses, the specimen develops cracks that already start from the first cycles, which expand in the

**Table 4** Stress cycle results Gyroid tested at impact heights at 0.6 m and 38.3 J

Gyroid 0.6 m – 38.3 J			
Number of cycles	Initial height (mm)	Height after impact (mm)	Height after shape recovery (mm)
1 <sup>st</sup> Cycle –	30.5	29.8	31.6
2 <sup>nd</sup> Cycle –	31.75	30.4	32
3 <sup>rd</sup> Cycle –	32	30.65	32.15
4 <sup>th</sup> Cycle	32.15	30.5	32.1
5 <sup>th</sup> Cycle –	32.1	30.25	32.05

last two cycles, in such a way as to prevent the structure from fully recovering both the height and the shape itself. In the fourth and fifth cycles, the damages caused by the impact cycles are, in fact, such that the post-recovery height is lower than the initial one, as the cracks created do not allow a total recovery of the shape.

Table 5 shows the values of the initial height, of the height after the impact and after the shape recovery, respectively, for impact tests carried out with a grave height of 0.8 m corresponding to 51.8 J. In this case, the Gyroid structure is able to withstand three cycles of stress—recovery

**Fig. 11** Selected geometries for the three impact energy categories

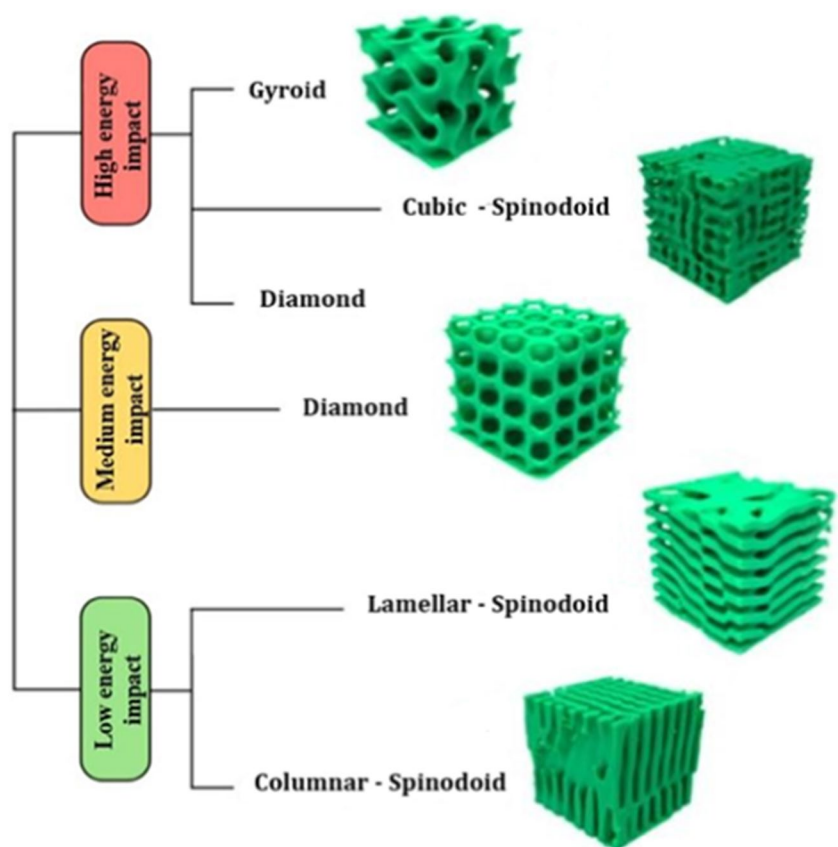


**Table 5** Stress cycle results Gyroid tested at impact heights at 0.8 m and 51.8 J

Gyroid 0.8 m – 51.8 J			
Number of cycles	Initial height (mm)	Height after impact (mm)	Height after shape recovery (mm)
1 <sup>st</sup> Cycle -	30.5	29	31.7
2 <sup>nd</sup> Cycle -	32	29.5	31.75
3 <sup>rd</sup> Cycle -	32	29.75	31.5

**Table 6** Stress cycle results Gyroid tested at impact heights at 0.9 m and 57.4 J

Gyroid 0.9 m – 57.4 J			
Number of cycles	Initial height (mm)	Height after impact (mm)	Height after shape recovery (mm)
1 <sup>st</sup> Cycle -	30.8	29.25	31.55
2 <sup>nd</sup> Cycle -	31.6	28.85	31.75

of the shape, thus highlighting a behaviour similar to that obtained for impacts at heights of 0.6 m.

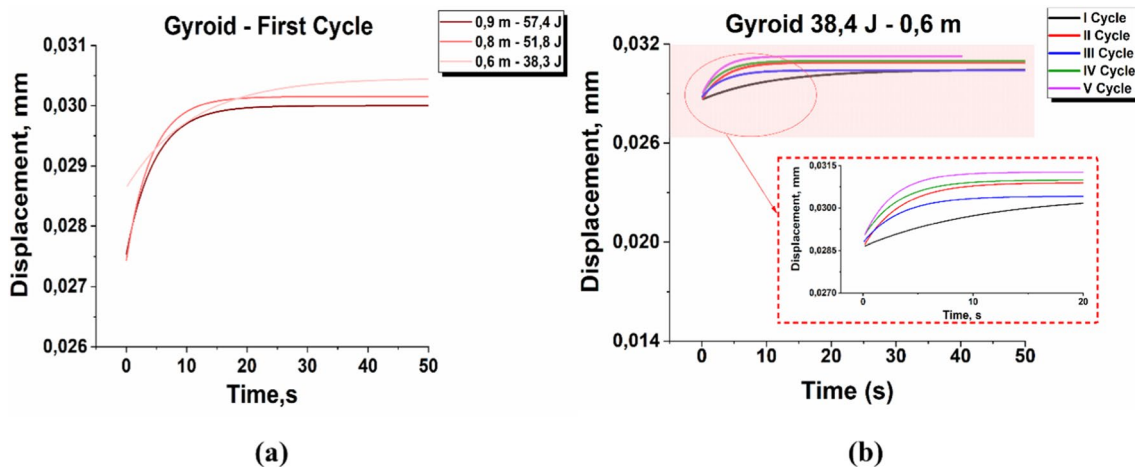
For impact tests with energy corresponding to 57.4 J, i.e. with a falling height of the body equal to 0.9 m, the structure breaks irreversibly already at the third impact, after the second shape recovery (Table 6).

Figure 12a illustrates the shape recovery trend during the first cycles at impact energies of 57.4 J, 51.8 J and 38.4 J. In the first cycle carried out at an impact height of 0.6 m, recovery occurs faster in the first five seconds, compared to tests carried out with impact heights of 0.8 m and 0.9 m.

Thereafter, recovery proceeds gradually up to approximately 20 s, with further height recovery over the remaining 25 s.

Figure 12b shows the time vs. displacement trends of the shape recovery for the cycles performed at impact heights of 0.6 m. The recovery speed is higher in the last recovery cycles due to the greater damage present in the structures tested. In the first cycles, particularly in the first cycle, the recovery speed is rather slow, with the maximum recovery occurring in about 40 s. For the subsequent cycles, the maximum recovery is reached before 20 s. The greater integrity of the structure during the first cycle makes recovery more complex by virtue of the greater mechanical resistance of the structure itself. When significant damage in the structure take place, such damage reduces the mechanical resistance of the structure and this allows an acceleration of the recovery process. Figure 13 shows the state of damage of the Gyroidal structure after the impacts at 0.6 m (a), 0.8 m (b) and 0.9 m (c), respectively. In all cases, it is evident that from the first impact cracks form, which subsequently widen in size as the number of cycles increases. It is important to note that the rate of crack expansion is closely related to the magnitude of the impact energy and the number of cycles.

Tables 7, 8 and 9 show the results of the stress cycles for the Cubic Spinoidal structure relating to the impact energies of 38.3 J, 51.8 J and 57.4 J. For impact heights of 0.6 m, the structure shows a limited deformation of about 0.2 mm, only in the first cycle. In subsequent cycles, the displacement increases until it exceeds 1.3 mm in the fourth cycle, where the structure is permanently deformed and can no longer be submitted to further cycles. These considerations can be extended to impact heights of 0.8 m. If the structure is submitted to an impact height of 0.9 m it is possible to carry out only one cycle, since for a second impact with an energy of 57.4 J the geometry breaks irreversibly.

**Fig. 12** a Recovery of shape of the first cycle performed at energies of 57.4 J, 51.8 J and 38.3 J, respectively, b Shape recovery cycles for impact heights of 0.6 m



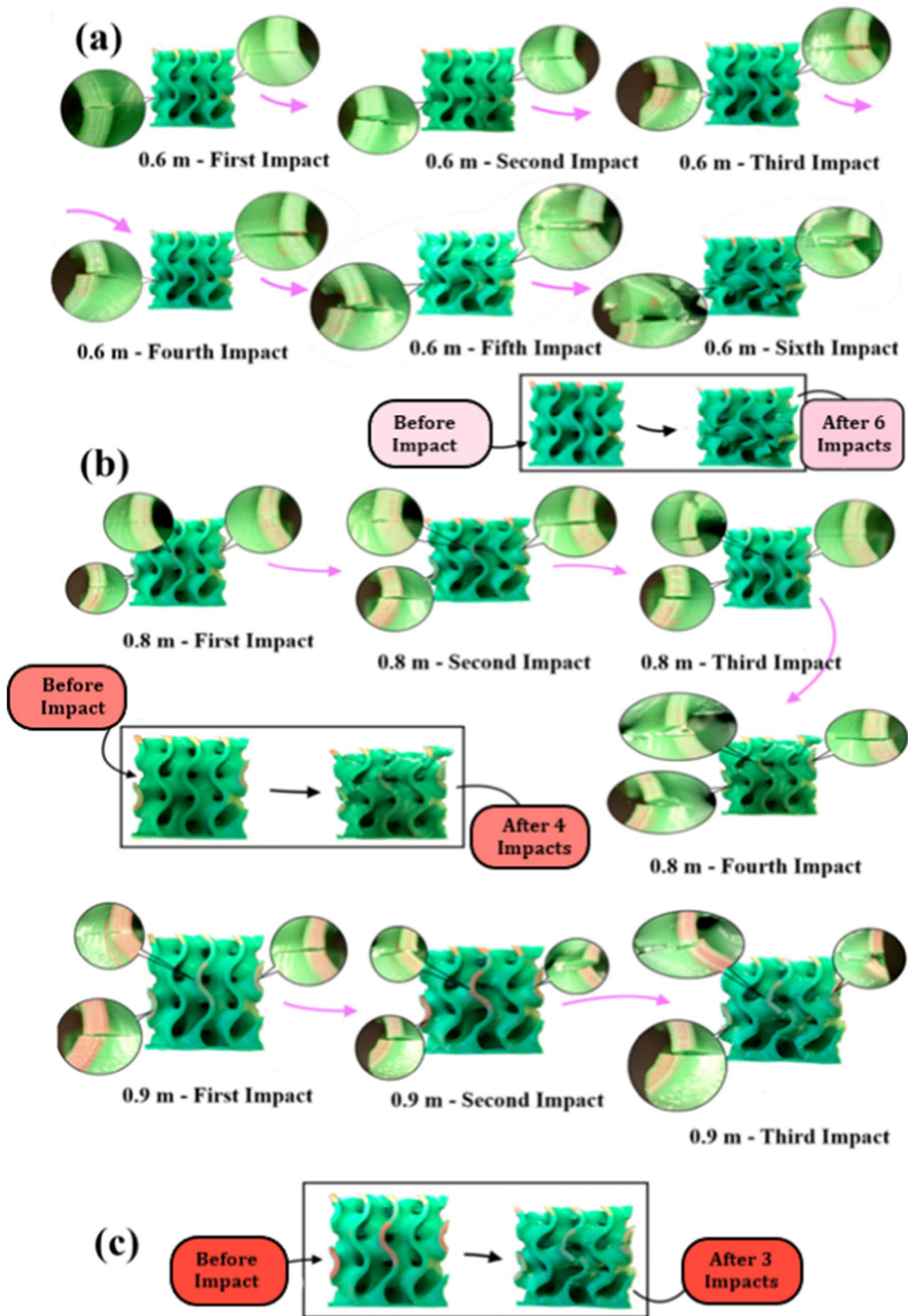


Fig. 13 Damage to the Gyroidal structure as the cycles vary for impacts of 0.6 m (a) 0.8 m (b) 0.9 m (c)

**Table 7** Stress cycle results of Cubic Spinoidal tested at impact heights at 0.6 m and 38.3 J

Cubic Spinodoid 0.6 m – 38.3 J			
Number of cycles	Initial height (mm)	Height after impact (mm)	Height after shape recovery (mm)
1 <sup>st</sup> Cycle –	30.5	30.3	31.25
2 <sup>nd</sup> Cycle –	31.35	30.7	31.5
3 <sup>rd</sup> Cycle –	31.6	30.65	31.65
4 <sup>th</sup> Cycle	31.7	30.45	31.4

**Table 8** Stress cycle results of Cubic Spinoidal tested at impact heights at 0.8 m and 51.8 J

Cubic Spinodoid 0.8 m – 51.8 J			
Number of cycles	Initial height (mm)	Height after impact (mm)	Height after shape recovery (mm)
1 <sup>st</sup> Cycle –	30.75	30	31.45
2 <sup>nd</sup> Cycle –	31.5	30	31
3 <sup>rd</sup> Cycle –	32.3	29.2	31.75

**Table 9** Stress cycle results of Cubic Spinoidal tested at impact heights at 0.9 m and 57.4 J

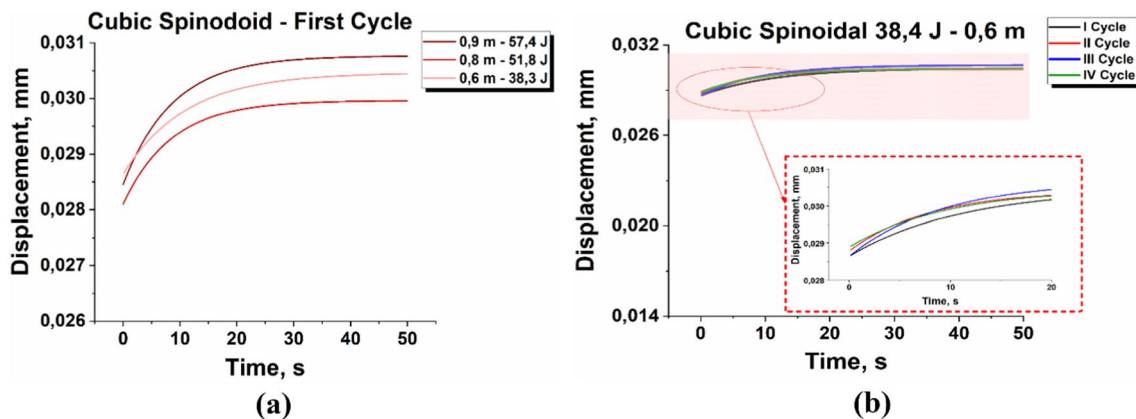
Cubic Spinodoid 0.9 m – 57.4 J			
Number of cycles	Initial height (mm)	Height after impact (mm)	Height after shape recovery (mm)
1 <sup>st</sup> Cycle –	30.75	29.45	31

The damage of the structure influences, as already seen previously, the recovery of the initial height. In the first recovery cycles, the resulting height is greater than the starting height. As the damage increases, the structure is unable to fully recover its shape and consequently the initial height is not restored. During the first cycles carried out at different impact energies, the Spinoidal structure shows a reduced displacement compared to that recorded in the case of the Gyroid structure. At the same time, the Gyroidal structure has a superior mechanical strength, allowing it to undergo a greater number of stress cycles—shape recovery. Also in [2] in the case of compressive stress, the Gyroid structure is competitive with the other periodic triple surface structures. It has superior mechanical strength and better absorption capacity for relative densities higher than 30%.

Figure 14a shows how the Spinoidal structure exhibits excellent behavior in the first cycle performed at 57.4 J, while recovery at 51.8 J and 38.3 J is reduced, as is the final height recovered. For impact heights of 0.6 m, the structure is able to withstand four recovery cycles. In this case, the recovery speed increases with the number of cycles, but it assumes comparable values for the final three cycles, as shown in Fig. 14b.

#### b Shape recovery cycles for impact heights of 0.6 m

With the increase of the impact energy, a greater interpenetration between the planes of the Cubic Spinoidal structure is observed, also due to the presence of a considerable amount of internal defects, as shown in Fig. 15. In the case of the Cubic Spinoidal structure, a clear influence of the internal defects with respect to the structural behaviour is highlighted. The Gyroidal structure guarantees better behaviour due to the lower presence of internal defects. Furthermore, the resistant section, although variable, remains almost constant as the number of cycles varies. The cubic

**Fig. 14** a Recovery of shape of the first cycle performed at energies of 57.4 J, 51.8 J and 38.3 J, respectively

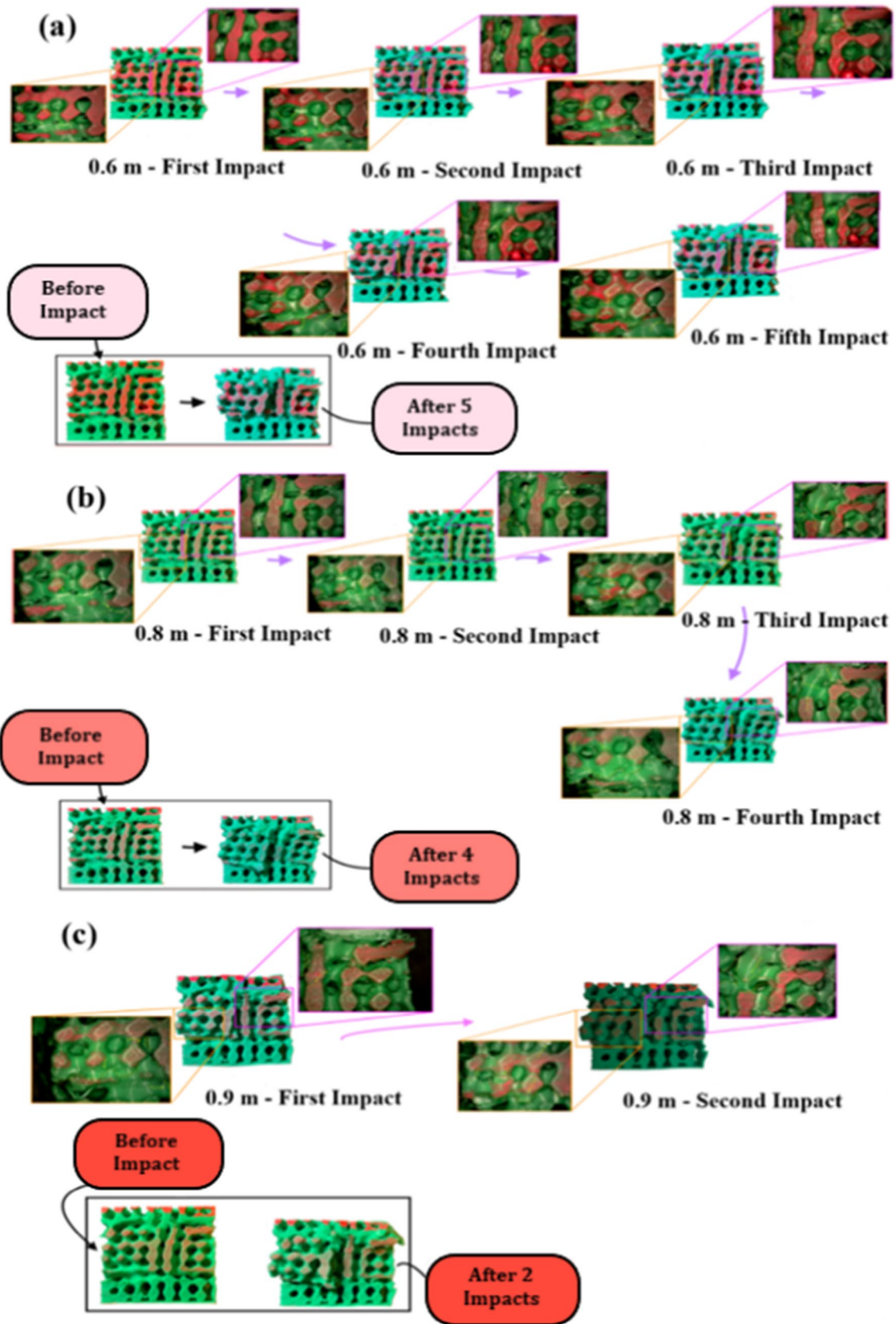


Fig. 15 Damage to the Spinoidal cubic structure as the cycles vary for impacts of 0.6 m (a), 0.8 m (b), 0.9 m (c)



Spinoidal structure is subject to more internal defects, which lead to a drastic reduction in its performance. In reality one of the main reasons for the failure of the Cubic Spinoidal structure is ascribable to the numerous internal cavities, where cracks can start and increase. This can lead the structure to collapse as an effect of the concentration of efforts. The Gyroid structure presents a gradual variation of shape.

This geometric feature is useful because it allows to avoid, at least partially, the concentration of stresses which would otherwise occur due to sudden variations in section. On the other hand, in the cubic Spinoidal structure there are sudden variations in section, which make it more vulnerable to the stresses of high-energy impacts. In fact, damage and failure begin to appear after the first impact at maximum energy due to sudden changes in the shape of the geometry. The first impact made with the impact height of 0.9 m and energy of 57.4 J produces different effects on the two structures. In the Gyroid structure, the first cracks are formed, which, as the number of cycles increases, tend to increase until they reach collapse. For the Cubic Spinoidal structure, this energy is already sufficient to bring part of the specimen to failure. As shown in Fig. 15, the Cubic Spinoidal structure presents a flaking of the planes with loss of the original shape. Furthermore, cracks are triggered within the structure.

Figure 16 shows the comparison between the two structures tested at high impact energies. The Spinoidal structure has an opening along the middle plane, unlike the Gyroid structure, which shows a similar deformation on all faces. The Spinoidal structure shows lower performance than the Gyroidal structure, as it is able to withstand fewer cycles of stress – recovery of shape.

### 3.2.2 Structures with medium impact energy

As earlier mentioned, the Diamond structure was, during the first step of the experimental investigation, classified in the category of medium impact energy structures. Despite this, the Diamond structure was also tested at impact heights of fall of 0.8 and 0.9 m, respectively, this because of the limited deformation found for energies lower than 40 J.

Tables 10, 11 and 12 show the results of cyclic tests performed at medium energy levels for the Diamond structure. For impact energies of 25.5 J, the displacement detected is small and less than 1 mm up to the seventh cycle. In the last three cycles, the state of damage is such as not to allow a complete recovery of the original height. Despite this, the difference between the post recovery height and the initial height is limited, settling at 0.75 mm in the last cycle. For impact heights of 0.5 and 0.6 m, the structure resisted

**Table 10** Diamond stress cycle results tested at impact heights at 0.4 m and 25.5 J

Diamond 0.4 m – 25.5 J			
Number of cycles	Initial height (mm)	Height after impact (mm)	Height after shape recovery (mm)
1 <sup>st</sup> Cycle –	30.65	30.25	31.7
2 <sup>nd</sup> Cycle –	31.75	31	31.75
3 <sup>rd</sup> Cycle –	31.75	30.85	31.9
4 <sup>th</sup> Cycle	31.95	31.2	32.25
5 <sup>th</sup> Cycle –	32.3	31.45	32.3
6 <sup>th</sup> Cycle	32.35	31.3	32.25
7 <sup>th</sup> Cycle	32.3	31.45	32.2

**Fig. 16** Comparison of Gyroid and Cubic Spinoidal structure for different energy levels, following shape recovery

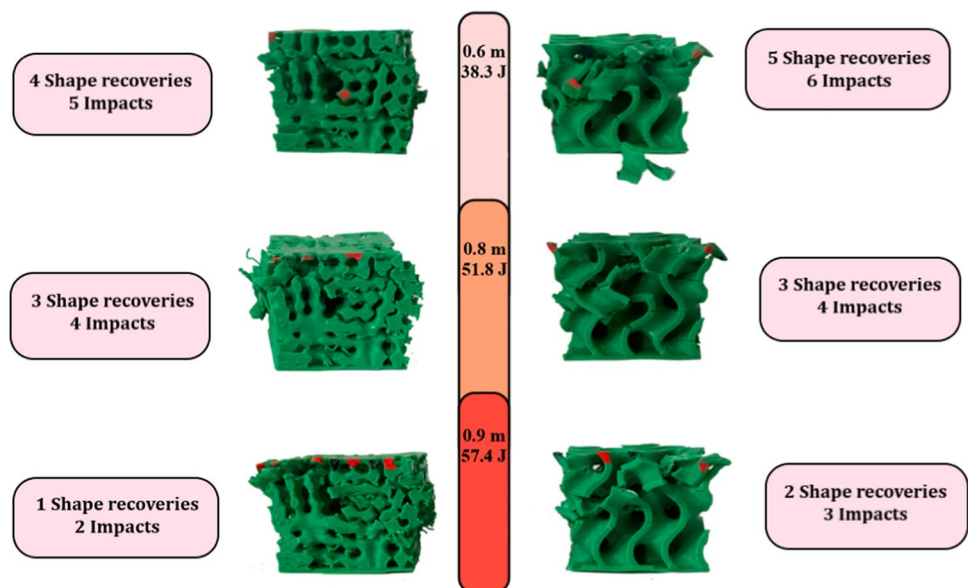




**Table 11** Diamond stress cycle results tested at impact heights at 0.5 m and 31.9 J

Diamond 0.5 m – 31.9 J			
Number of cycles	Initial height (mm)	Height after impact (mm)	Height after shape recovery (mm)
1 <sup>st</sup> Cycle –	30.65	30.05	31.6
2 <sup>nd</sup> Cycle –	31.75	31	31.95
3 <sup>rd</sup> Cycle –	32	30.9	32.15
4 <sup>th</sup> Cycle	32.2	30.8	32.45
5 <sup>th</sup> Cycle –	32.5	30.75	32.6

**Table 12** Diamond stress cycle results tested at impact heights at 0.6 m and 38.3 J

Diamond 0.6 m – 38.3 J			
Number of cycles	Initial height (mm)	Height after impact (mm)	Height after shape recovery (mm)
1 <sup>st</sup> Cycle –	30.75	29.75	31.5
2 <sup>nd</sup> Cycle –	31.65	30	31.7
3 <sup>rd</sup> Cycle –	31.7	30	31.75

**Table 13** Diamond stress cycle results tested at impact heights at 0.8 m and 51.8 J

Diamond 0.8 m – 51.8 J			
Number of cycles	Initial height (mm)	Height after impact (mm)	Height after shape recovery (mm)
1 <sup>st</sup> Cycle –	30.75	29.35	31.55
2 <sup>nd</sup> Cycle –	31.7	28.9	31.5

respectively 5 cycles and 3 cycles, proving to be the best choice for the category of medium impact energy structures.

Subsequently, the Diamond structure was submitted to impact energies of 51.8 J and 57.4 J, respectively. From the experimental results shown in Tables 13 and 14, the strength of the structure decreases significantly, especially for impact heights of 0.9 m (that is, at the highest impact energy). At this impact height, the structure was unable to withstand even after the first cycle of stress and recovery, completely yielding to the applied load.

Figure 17a and b show the displacement vs. time curves relating to shape recovery for the first cycles performed at different energy levels and for the cycles performed at the minimum impact height of 0.4 m. For impacts made at 0.4 and 0.5 m, recovery occurs quickly in the first 10 s compared to the other impact energy levels. Subsequently, in the

**Table 14** Diamond stress cycle results tested at impact heights at 0.9 m and 57.4 J

Diamond 0.9 m – 57.4 J			
Number of cycles	Initial height (mm)	Height after impact (mm)	Height after shape recovery (mm)
1 <sup>st</sup> Cycle –	30.75	28.6	31.55

remaining 30 s, the recovery keeps on being observed. In the higher energy levels, the recovery speed is instead almost constant, especially for 51.8 J and 38.3 J.

For the cycles performed at 25.5 J, during the first cycles the structure takes longer to restore the initial configuration. During subsequent cycles, recovery begins approximately 5 s after the material has been placed in the thermostat bath. This suggests, as previously discussed, that damage to the material hinders the recovery of the initial shape and that the water present plays an important role in the recovery process, thanks to the hydrostatic pressure acting on the structure. Thermal recovery is effective for restoring connections that have undergone significant bending, but which have not fractured yet. In the last few cycles, most of the arms connecting the cells break, reducing the number of connections through which the impact energy is distributed. This leads to a higher local stress generated, with a significantly more intense effect. Therefore, a slight increase in load is enough to reduce the number of stress cycles.

Figure 18 compares the results obtained on five different specimens as the impact energy varies, when the structures reach a status of permanent failure. Furthermore, the different fracture conditions generated on the specimen starting from a minimum load of 25.5 J up to a maximum of 57.4 J are highlighted. The Diamond structure does not appear to be suitable for operating at high impact energies. On the contrary, its performances are very good for medium impact energy and lower than 40 J.

### 3.2.3 Structures with low impact energy

For Spinoidal Lamellar structure, the cyclic tests were conducted at impact energies of 12.7 J, 19.1 J and 25.5 J, with the results being reported in Tables 15, 16 and 17, respectively. For impact heights of 0.2 m, an 11% reduction in specimen height was observed from the first cycle to the eighth. In these tests, the deformation measurement is not linked to the failure of the specimen, but the test is interrupted when the deformation causes a reduction in the height of the specimen greater than 10% with respect to the starting one. The Lamellar structure favours the recovery of shape, which for each cycle is between 2 and 3 mm. For higher impact energies, for example 25.5 J, the structure is unable

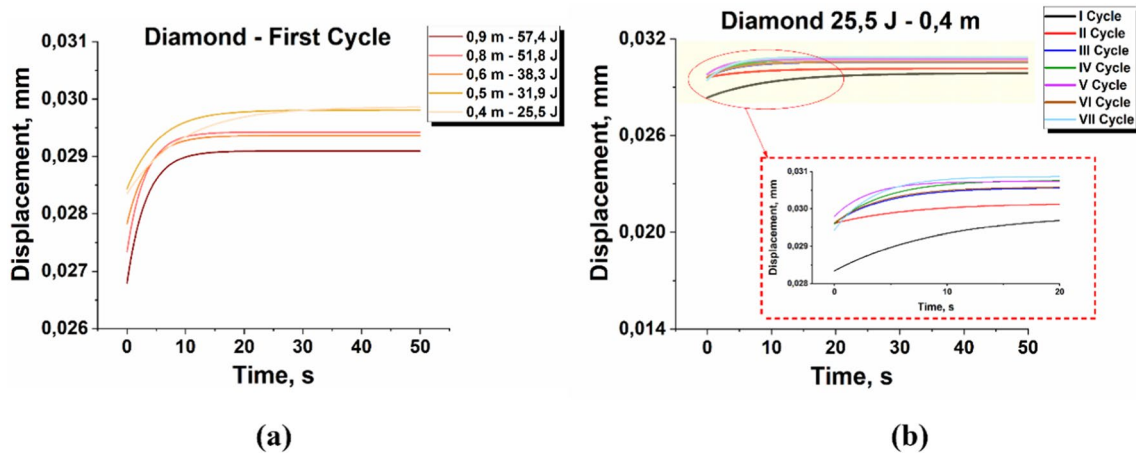


**Fig. 17** a Shape recovery of the first cycle carried out respectively at energies of 57.4 J, 51.8 J, 38.3 J, 31.9 J and 25.5 J. b Shape recovery cycles for impact heights equal to 0.4 m

**Fig. 18** Comparison of diamond structure at various energy levels and impact heights

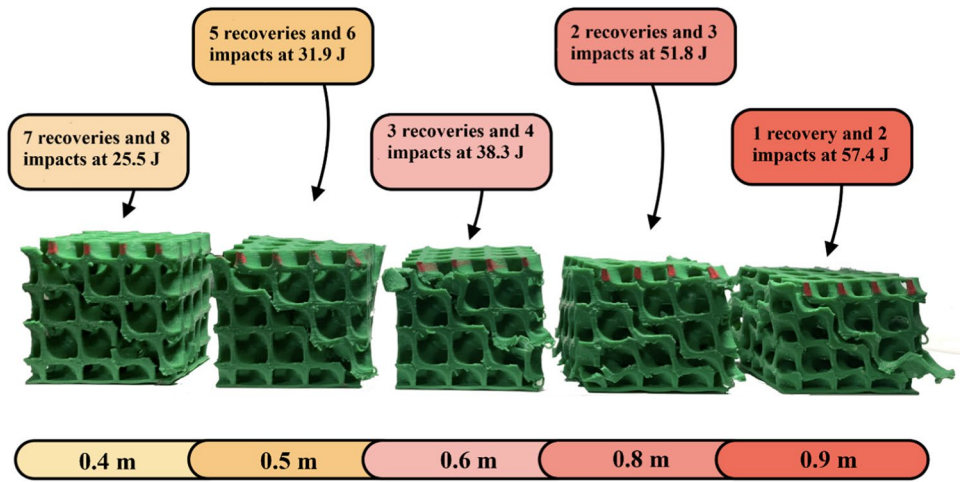


**Table 15** Stress cycle results of the Lamella Spinoidal tested at impact heights at 0.2 m and 12.7 J

Lamellar Spinodoid 0.2 m – 12.7 J			
Number of cycles	Initial height (mm)	Height after impact (mm)	Height after shape recovery (mm)
1 <sup>st</sup> Cycle –	30.25	28.2	29.45
2 <sup>nd</sup> Cycle –	29.25	26.9	28.2
3 <sup>rd</sup> Cycle –	28.3	25.75	28.15
4 <sup>th</sup> Cycle	28.25	26.1	28.15
5 <sup>th</sup> Cycle –	28.3	25.9	28.1
6 <sup>th</sup> Cycle	28.16	26.2	27.55
7 <sup>th</sup> Cycle	27.6	26.1	27.2
8 <sup>th</sup> Cycle	27.28	25.7	27.04

**Table 16** Stress cycle results of the Lamellar Spinoidal tested at impact heights at 0.3 m and 19.1 J

Lamellar Spinodoid 0.3 m – 19.1 J			
Number of cycles	Initial height (mm)	Height after impact (mm)	Height after shape recovery (mm)
1 <sup>st</sup> Cycle –	31	26.7	28.9
2 <sup>nd</sup> Cycle –	28.95	25.5	28.35
3 <sup>rd</sup> Cycle –	28.4	25	28.1
4 <sup>th</sup> Cycle	28.2	24.8	27.9
5 <sup>th</sup> Cycle –	28	24.65	27.8
6 <sup>th</sup> Cycle	27.85	24.1	27.2
7 <sup>th</sup> Cycle	27.2	23.5	26.6

**Table 17** Stress cycle results of the Lamellar Spinoidal tested at impact heights at 0.4 m and 25.5 J

Lamellar Spinodoid 0.4 m – 25.5 J			
Number of cycles	Initial height (mm)	Height after impact (mm)	Height after shape recovery (mm)
1 <sup>st</sup> Cycle –	30.95	25.05	27.7
2 <sup>nd</sup> Cycle –	27.8	23.1	26.2

to withstand the stress and carry out the recovery phase for more than 2 cycles. This is due to the high packing to which the structure is subjected, which causes a significant loss of its recovery capacity and affects its mechanical strength.

Figure 19 shows the trend of the displacement vs. time curves for the first cycles performed at 25.5 J, 19.1 J and 12.7 J (a), respectively, and of the cycles performed at an impact energy of 12.7 J (b). For the first cycles carried out with low energy, the recovery speed is limited, with the height being restored in less than 5 s. When the impacts occur at impact heights of 0.4 m, the final height is recovered only 30 s after the dipping of the sample in the thermostatic bath.

Figure 19b confirms how in the first stress cycles the recovery speed is almost instantaneous and increases as the number of cycles increases. The speed of recovery also increases as the level of damage to the structure increases, as previously discussed.

Tables 18, 19 and 20 show the results of the impact tests conducted at 12.7 J, 19.1 J and 25.5 J, respectively. The variation between the initial height, the height after the impact and the height after the recovery is always rather limited, reaching a maximum of 0.5 mm. This means that the deformation that took place are rather small, too.

**Table 18** Stress cycle results of the Columnar Spinoidal tested at impact heights at 0.2 m and 12.7 J

Spinodoid Columnar 0.2 m – 12.7 J			
Number of cycles	Initial height (mm)	Height after impact (mm)	Height after shape recovery (mm)
1 <sup>st</sup> Cycle –	30.25	30.1	31.5
2 <sup>nd</sup> Cycle –	31.6	31.2	31.5
3 <sup>rd</sup> Cycle –	31.55	31.4	31.75
4 <sup>th</sup> Cycle	31.8	31.55	31.65
5 <sup>th</sup> Cycle –	31.7	31.5	31.6
6 <sup>th</sup> Cycle	31.7	31.55	31.65
7 <sup>th</sup> Cycle	31.7	31.6	31.75
8 <sup>th</sup> Cycle	31.8	31.7	31.8

For impact energies of 25.5 J, the structure is able to withstand 5 load—recovery cycles. On the sixth impact, the structure exhibits an irreversible break, without the possibility of being tested again.

Figure 20a shows the time vs. displacement curves for the first cycles performed at different impact heights: 0.2 m, 0.3 m and 0.4 m. The recovery speed is very similar in the three cases, with recovery times increasing as the damage to the structure increases. As regards the cycles carried out with an impact energy of 12.7 J, as shown in Fig. 20b, the recovery speed does not show a particular trend, remaining limited for all the stress cycles. This suggests that the columnar structure, when submitted to this specific impact energy, maintains a good recovery capacity, with relatively stable and limited recovery times.

The two structures show divergent behaviour, making it difficult to define which geometry is better. The Lamellar Spinoidal structure has a more open structure

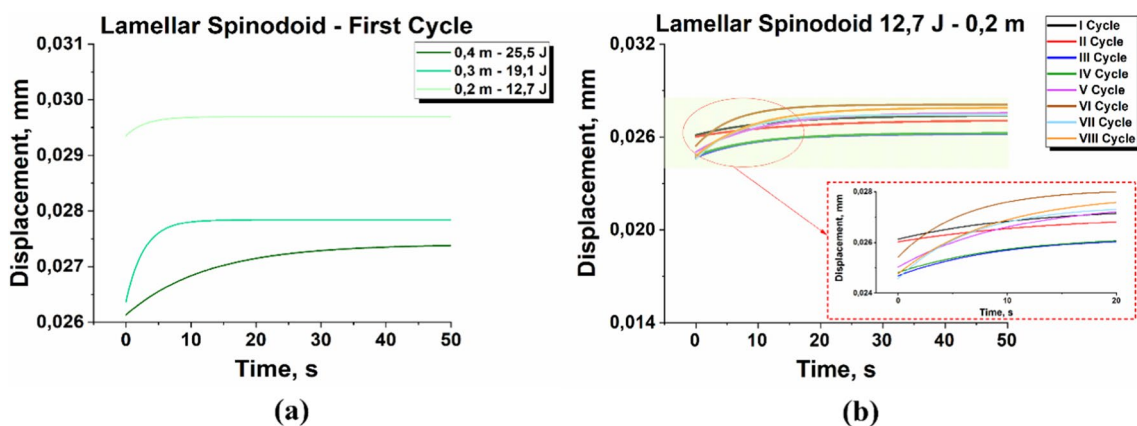


**Fig. 19** a Shape recovery of the first cycle carried out respectively at energies of 25.5 J, 19.1 J and 12.7 J. b Shape recovery cycles for impact heights equal to 0.2 m

**Table 19** Stress cycle results of the Columnar Spinoidal tested at impact heights at 0.3 m and 19.1 J

Spinoid Columnar 0.3 m – 19.1 J			
Number of cycles	Initial height (mm)	Height after impact (mm)	Height after shape recovery (mm)
1 <sup>st</sup> Cycle –	30.5	30.3	31.3
2 <sup>nd</sup> Cycle –	31.35	31.15	31.35
3 <sup>rd</sup> Cycle –	31.4	31.2	31.4
4 <sup>th</sup> Cycle	31.45	31.15	31.45
5 <sup>th</sup> Cycle –	31.5	31.3	31.6
6 <sup>th</sup> Cycle	31.65	31.5	31.6
7 <sup>th</sup> Cycle	31.7	31.6	31.65
8 <sup>th</sup> Cycle	31.65	31.55	31.75

**Table 20** Stress cycle results of the Columnar Spinoidal tested at impact heights at 0.4 m and 25.5 J

Spinoid Columnar 0.4 m – 25.5 J			
Number of cycles	Initial height (mm)	Height after impact (mm)	Height after shape recovery (mm)
1 <sup>st</sup> Cycle –	30.5	30.25	31.45
2 <sup>nd</sup> Cycle –	31.5	31.35	31.3
3 <sup>rd</sup> Cycle –	31.3	31.25	31.4
4 <sup>th</sup> Cycle	31.45	31.3	31.5
5 <sup>th</sup> Cycle –	31.55	31.25	31.65

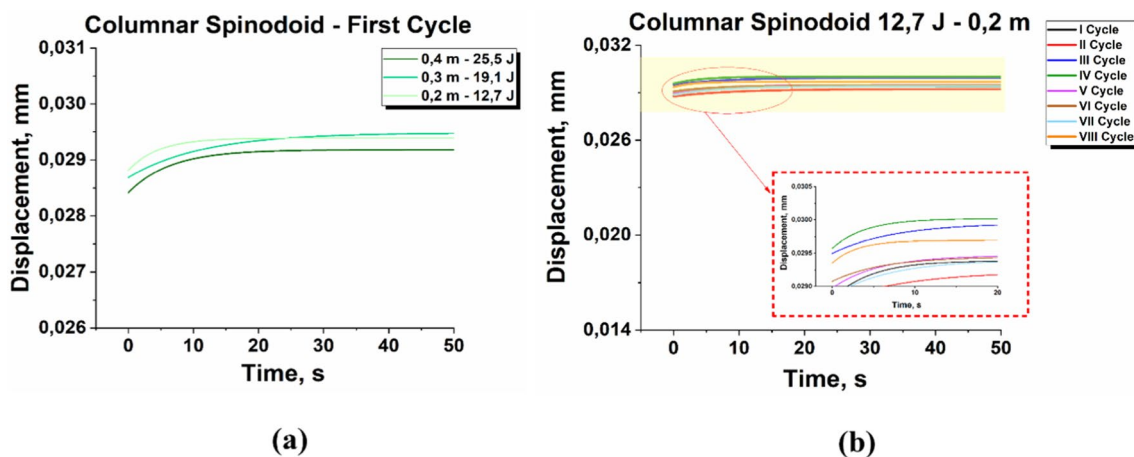
and this guarantees greater recovery both in terms of height variation and speed. However, as cycles go by, the height change between cycles decreases until the structure reaches a point, where it shows "packing".

In this phase, the geometry of the structure become very compact, reducing its damping capacity. As a result, when the structure is packed, it does not have a high strength and the cracks propagate rapidly without leading to complete failure of the structure.

The Lamellar structure shows a remarkable plasticization without showing signs of breakage, despite the repeated stresses applied. This is highlighted in Fig. 21, where the geometry can be seen after the first impact and after the eighth impact, both with an impact energy of 12.7 J.

For the Spinoidal Columnar structure, the plastic deformation is almost absent, therefore the shape recovery is rather limited, both in terms of stroke and speed. The structure exploits its ability to dampen the impact by bending laterally, thanks to the vertical arrangement of the elements with respect to the applied stress, as opposed to the lamellar geometry where the elements are arranged orthogonally. This aspect allows the Spinoidal Columnar structure to resist numerous load applications before reaching failure, until a critical load is reached. Beyond this critical load, the failure is sudden and catastrophic, differently from what is observed in the Lamellar structure. Figure 22 shows how for impacts at 25.5 J, the specimen shows no signs of yielding in the third and fourth cycle performed. Furthermore, when it breaks in the last cycle, it maintains a height similar to the starting one. This can also be attributed to the fact that the recovery phases tend to inflate the structure, which undergoes a minimum height variation during the subsequent impact.

Figure 23 shows the shape recoveries of high-energy impact structures such as the Gyroid and the Spinoidal Cubic. Figure 23 also shows the shape recoveries of medium-energy impact structures as the Diamond and low-energy impact structures as the Spinoidal Lamellar and Columnar. The frames shown refer to the start of the test (Fig. 23a, d, g, l and o), after 9 s (Fig. 23b, e, h, m

**Fig. 20** **a** Shape recovery of the first cycle carried out respectively at energies of 25.5 J, 19.1 J and 12.7 J. **b** Shape recovery cycles for impact heights equal to 0.2 m



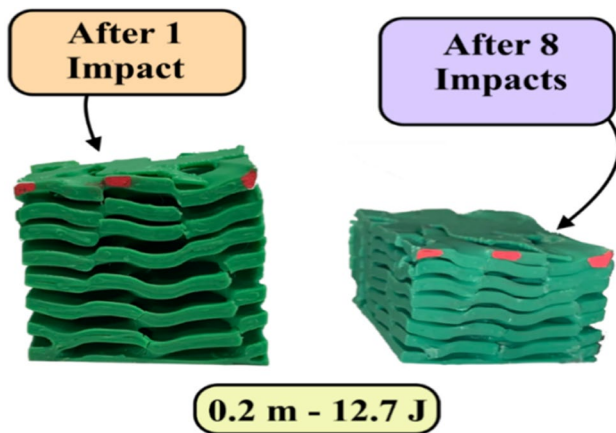


**Fig. 21** Spinoidal Lamellar deformation after 1 impact and 8 impacts at impact energies of 12.7 J

and p) and at the end of the test (Fig. 23c, f, i, n and q), respectively. For all the structures the first cycle involved impact energies of 38.4 J for the Gyroid and the Spinoidal Cubic, 25.5 J for the Diamond and 12.7 J for the Lamellar and Columnar Spinoidal structure, respectively.

In Table 21 the results of the experiment are reported reporting the type of structure, the density, the level of impact energy, the maximum number of cycles endurable by the structure, the maximum level of energy, the type of damage and future applications.

### 4 Conclusions

In this research the behaviour of three different types of cellular structures is analysed once submitted to impact stress and subsequent recovery of the shape. The investigated

structures were classified into three categories: Strut-based, Surface-based TPMS and Spinoidal. Three categories of impact tests were defined, using high, medium and low impact energy. The impact tests allowed the identification of the optimal combination between impact height and impact energy. This approach was found to allow the samples to undergo elastic deformations or, at most, small plastic deformations. Subsequently, for each category, the structures with the best behaviour in the impact test were selected and submitted to repeated cycles of load and shape recovery by applying an external thermal stimulus. It is worthwhile mentioning that to restore the shape, water at a temperature above the glass transition of PLA was considered in the present analysis, although future studies will focus on different and more practical heat source such as hot guns that provide a uniformly distributed flow of hot air on the samples.

The Gyroid and Cubic Spinoidal structures are the structures selected for the high impact energy category, whose behaviour was influenced by the presence of internal defects. The Gyroidal structure showed a better behaviour thanks also to a limited presence of internal defects, contrary to the Spinoidal structure in which the defects are intrinsic to the manufacturing process. The Surface-based structure also boasted a high mechanical resistance, allowing it to undergo a greater number of stress cycles—recovery of the shape. The Diamond structure is the best for medium impact energy, while it shows poor performance for higher energies. For low impact energy, the Columnar structure deforms little plastically, resulting in limited recovery of shape and height. On the contrary, the Lamellar structure undergoes more plastic deformations. For all the geometries selected, a correlation between the number of cycles and recovery speed was found. For small number of fractures, that is for a small number of cycles, the recovery speed was found to

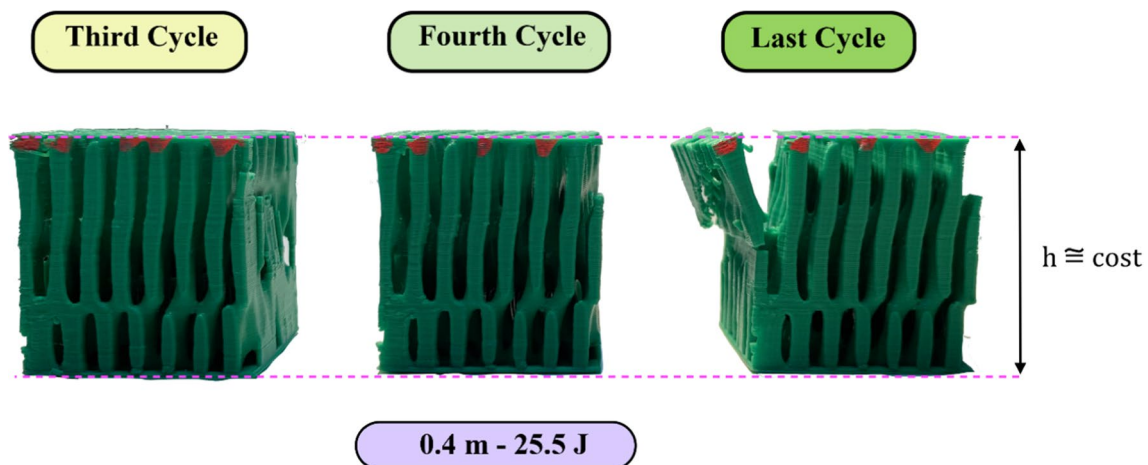


**Fig. 22** Spinoidal columnar deformation at the third, fourth and fifth cycles for impact energies of 25.5 J

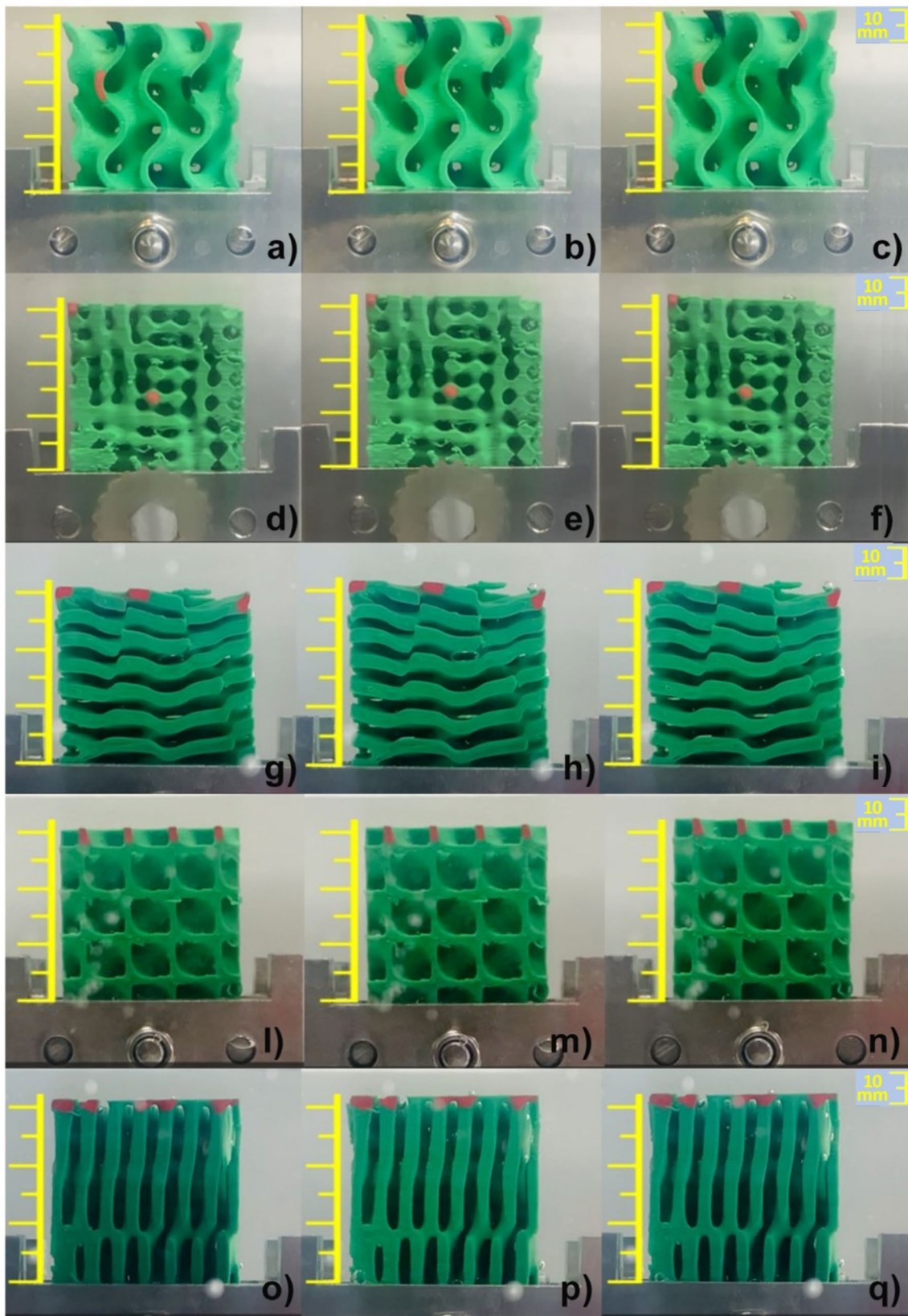


**Fig. 23** Shape recovery of the structures analysed at the start of the test (**a**), (**d**), (**g**), (**l**) and (**o**), after 9 s (**b**), (**e**), (**h**), (**m**) and (**p**) and at the end of the test (**c**), (**f**), (**i**), (**n**) and (**q**)

**Table 21** Summary table of research results

Structures	Density	Impact Energy	Max number of cycles	Max energy, (J)	Max height recovered (mm)	Damage Type	Future applications
Gyroid (TPMS)	0.3	High	5	57.4	2.9	Slots that increase in size as the number of cycles increases	Manufacture of deformable parts of cars, such as bumpers [51]
Diamond (TPMS)	0.3	High	2	57.4	1.85	Breaking of the connecting arms between the cells as the number of cycles increases	Suitable for transport applications such as packaging [28]
Diamond (TPMS)	0.3	Medium	2/7	38.3	2.95	Breaking of the connecting arms between the cells as the number of cycles increases	Suitable for transport applications such as packaging [28]
Cubic (Spinodoid)	0.5	High	4	57.4	2.55	Internal defects that widen with the increase of the cycles and interpenetration of the plans	Manufacture of motorcycle and safety helmets for major impacts
Lamellar (Spinodoid)	0.5	Low	7	25.5	3.15	Mostly plastic deformation as the cycles increase: the structure tends to "bundle", with a reduction in mechanical strength	Manufacture of motorcycle and safety helmets for medium and low impact
Columnar (Spinodoid)	0.5	Low	8	25.5	1.4	Mostly elastic deformation, limited shape recovery and sudden rupture during the last cycle	

be almost instantaneous, assisted by the hydrostatic pressure of the water bath. The level of damage was also found to influence the final recovery height, which is higher than the starting one, especially for the first cycles. The only exception is shown by the Spinoidal lamellar structure, in which the packing effect of the structure reduces the resilience of the structure.

The structures selected after the first impact tests appear to be suitable for cyclic load tests and shape recovery, apart from the Cubic Spinoidal structure, in which the manufacturing process affects the mechanical response of the structure. Spinoidal structures, despite having a higher density, are more sensitive to cyclic impact and less inclined to fully recover their shape. They have considerable limitations due to their full-empty geometrical arrangement. The Strut-based structure, despite having the same density, are not suitable for this type of test. Conversely, TPMS structures are the most reliable and resistant to the repeated load cycles. In all cases, the level of damage was found to affect both the recovery extent and speed. When the damage of the

structure is higher, the recovery speed is reduced, with the exception of the Lamellar structure, which, due to its deformation mode, does not have a high mechanical resistance and is not able to fully recover its shape.

In conclusion, the experimental findings achieved provide the basis for forthcoming investigations, which will be focused on prototypes that will feature larger life cycles as well as higher strength and durability.

**Authors' contributions** All authors contributed equally to each part of this study conception and design. The first draft of the manuscript was written by Desole Maria Pia and all authors commented on previous versions of the manuscript. All authors read and approved the final manuscript.

**Funding** Open access funding provided by Università degli Studi Roma Tre within the CRUI-CARE Agreement. The authors did not receive funding.



## Declarations

**Conflicts of interest** The authors have no relevant financial or non-financial interests to disclose.

**Open Access** This article is licensed under a Creative Commons Attribution 4.0 International License, which permits use, sharing, adaptation, distribution and reproduction in any medium or format, as long as you give appropriate credit to the original author(s) and the source, provide a link to the Creative Commons licence, and indicate if changes were made. The images or other third party material in this article are included in the article's Creative Commons licence, unless indicated otherwise in a credit line to the material. If material is not included in the article's Creative Commons licence and your intended use is not permitted by statutory regulation or exceeds the permitted use, you will need to obtain permission directly from the copyright holder. To view a copy of this licence, visit <http://creativecommons.org/licenses/by/4.0/>.

## References

- Abou-Ali AM, Lee D-W, Abu Al-Rub RK (2022) On the effect of lattice topology on mechanical properties of SLS additively manufactured sheet-, ligament-, and strut-based polymeric metamaterials. *Polymers* 14:4583. <https://doi.org/10.3390/polym14214583>
- Abueidda DW, Elhebeary M, Shiang C-SA, Pang S, Abu Al-Rub RK, Jasiuk IM (2019) Mechanical properties of 3D printed polymeric Gyroid cellular structures: Experimental and finite element study. *Mater Des* 165:107597. <https://doi.org/10.1016/j.matdes.2019.107597>
- Al-Ketan O, Abu Al-Rub RK (2021) MSLattice: A free software for generating uniform and graded lattices based on triply periodic minimal surfaces. *Mater Des Process Commun* 3:e205. <https://doi.org/10.1002/mdp2.205>
- Andrew JJ, Schneider J, Ubaid J, Velmurugan R, Gupta NK, Kumar S (2021) Energy absorption characteristics of additively manufactured plate-lattices under low-velocity impact loading. *Int J Impact Eng* 149:103768. <https://doi.org/10.1016/j.ijimpeng.2020.103768>
- Azzouz L, Chen Y, Zarrelli M, Pearce JM, Mitchell L, Ren G, Grasso M (2019) Mechanical properties of 3-D printed truss-like latex biopolymer non-stochastic structures for sandwich panels with natural fiber composite skins. *Compos Struct* 213:220–230. <https://doi.org/10.1016/j.compstruct.2019.01.103>
- Babae S, Shim J, Weaver JC, Chen ER, Patel N, Bertoldi K (2013) 3D soft metamaterials with negative poisson's ratio. *Adv Mater* 25:5044–5049. <https://doi.org/10.1002/adma.201301986>
- Barletta M, Gisario A, Mehrpouya M (2021) 4D printing of shape memory polylactic acid (PLA) components: Investigating the role of the operational parameters in fused deposition modeling (FDM). *J Manuf Process* 61:473–480. <https://doi.org/10.1016/j.jmapro.2020.11.036>
- Bückmann T, Stenger N, Kadic M, Kaschke J, Frölich A, Kennerknecht T, Eberl C, Thiel M, Wegener M (2012) Tailored 3D mechanical metamaterials made by dip-in direct-laser-writing optical lithography. *Adv Mater* 24:2710–2714. <https://doi.org/10.1002/adma.201200584>
- Callister WD, Rethwisch DG (2012) *Materials science and engineering. An introduction*. Wiley, Hoboken, New Jersey, USA
- Champeau M, Heinze DA, Viana TN, de Souza ER, Chinellato AC, Titotto S (2020) 4D printing of hydrogels: A review. *Adv Func Mater* 30:1910606. <https://doi.org/10.1002/adfm.201910606>
- Cao D (2023) Investigation into surface-coated continuous flax fiber-reinforced natural sandwich composites via vacuum-assisted material extrusion. *Prog Addit Manuf*. <https://doi.org/10.1007/s40964-023-00508-6>
- Cao D (2023) Fusion joining of thermoplastic composites with a carbon fabric heating element modified by multiwalled carbon nanotube sheets. *Int J Adv Manuf Technol* 128:4443–4453. <https://doi.org/10.1007/s00170-023-12202-6>
- Cao D, Bouzolin D, Lu H, Griffith DT (2023) Bending and shear improvements in 3D-printed core sandwich composites through modification of resin uptake in the skin/core interphase region. *Compos B Eng* 264:110912. <https://doi.org/10.1016/j.compositesb.2023.110912>
- Davami K, Mohsenizadeh M, Munther M, Palma T, Beheshti A, Momeni K (2019) Dynamic energy absorption characteristics of additively manufactured shape-recovering lattice structures. *Mater Res Express* 6:045302. <https://doi.org/10.1088/2053-1591/aaf78c>
- Forés-Garriga A, Gómez-Gras G, Pérez MA (2022) Mechanical performance of additively manufactured lightweight cellular solids: Influence of cell pattern and relative density on the printing time and compression behavior. *Mater Des* 215:110474. <https://doi.org/10.1016/j.matdes.2022.110474>
- Fu K, Zhao Z, Jin L (2019) Programmable granular metamaterials for reusable energy absorption. *Adv Func Mater* 29:1901258. <https://doi.org/10.1002/adfm.201901258>
- Ge Q, Qi HJ, Dunn ML (2013) Active materials by four-dimension printing. *Appl Phys Lett* 103:131901. <https://doi.org/10.1063/1.4819837>
- Gisario A, Desole MP, Mehrpouya M, Barletta M (2023) Energy absorbing 4D printed meta-sandwich structures: load cycles and shape recovery. *Int J Adv Manuf Technol* 127:1779–1795. <https://doi.org/10.1007/s00170-023-11638-0>
- Güden M, Alpkaya AT, Hamat BA, Hızlı B, Taşdemirci A, Tanrikulu AA, Yavaş H (2022) The quasi-static crush response of electron-beam-melt body-centred Ti6Al4V - cubic lattices: The effect of the number of cells, strut diameter and face sheet. *Strain* 58:e12411. <https://doi.org/10.1111/str.12411>
- Hangai Y, Saito K, Utsunomiya T, Kuwazuru O, Yoshikawa N (2014) Fabrication and compression properties of functionally graded foam with uniform pore structures consisting of dissimilar A1050 and A6061 aluminum alloys. *Mater Sci Eng A* 613:163–170. <https://doi.org/10.1016/j.msea.2014.06.039>
- Heo Y, Sodano HA (2014) Self-healing polyurethanes with shape recovery. *Adv Func Mater* 24:5261–5268. <https://doi.org/10.1002/adfm.201400299>
- Huang WM, Ding Z, Wang CC, Wei J, Zhao Y, Purnawali H (2010) Shape memory materials. *Mater Today* 13:54–61. [https://doi.org/10.1016/S1369-7021\(10\)70128-0](https://doi.org/10.1016/S1369-7021(10)70128-0)
- Jackson JA, Messner MC, Dudukovic NA, Smith WL, Bekker L, Moran B, Golobic AM, Pascall AJ, Duoss EB, Loh KJ, Spadaccini CM (2018) Field responsive mechanical metamaterials. *Sci Adv* 4:eaa6419. <https://doi.org/10.1126/sciadv.aau6419>
- Jiang HY, Kelch S, Lendlein A (2006) Polymers move in response to light. *Adv Mater* 18:1471–1475. <https://doi.org/10.1002/adma.200502266>
- Jin N, Wang F, Wang Y, Zhang B, Cheng H, Zhang H (2019) Failure and energy absorption characteristics of four lattice structures under dynamic loading. *Mater Des* 169:107655. <https://doi.org/10.1016/j.matdes.2019.107655>
- Kansara H, Koh G, Varghese M, Luk JZX, Gomez EF, Kumar S, Zhang H, Martínez-Pañeda E, Tan W (2021) Data-driven modeling of scalable spinodoid structures for energy absorption. *Appl Phys*. <https://doi.org/10.48550/arXiv.2103.16292>



27. Kumar S, Tan S, Zheng L, Kochmann DM (2020) Inverse-designed spinoid metamaterials. *npj Comput Mater* 6:1–10. <https://doi.org/10.1038/s41524-020-0341-6>
28. Laskowska D, Szatkiewicz T, Bałasz B, Mitura K (2023) Mechanical properties and energy absorption abilities of diamond TPMS cylindrical structures fabricated by selective laser melting with 316L stainless steel. *Materials* 16:3196. <https://doi.org/10.3390/ma16083196>
29. Lee J-H, Singer JP, Thomas EL (2012) Micro-/Nanostructured mechanical metamaterials. *Adv Mater* 24:4782–4810. <https://doi.org/10.1002/adma.201201644>
30. Lendlein A, Jiang H, Jünger O, Langer R (2005) Light-induced shape-memory polymers. *Natures* 434:879–882. <https://doi.org/10.1038/nature03496>
31. Lendlein A, Kelch S (2002) Shape-memory polymers. *Angew Chem Int Ed* 41:2034–2057. [https://doi.org/10.1002/1521-3773\(20020617\)41:12%3c2034::AID-ANIE2034%3e3.0.CO;2-M](https://doi.org/10.1002/1521-3773(20020617)41:12%3c2034::AID-ANIE2034%3e3.0.CO;2-M)
32. Leng J, Lu H, Liu Y, Huang WM, Du S (2009) Shape-memory polymers—a class of novel smart materials. *MRS Bull* 34:848–855. <https://doi.org/10.1557/mrs2009.235>
33. Lesmana LA, Lu C, Chen F, Aziz M (2023) Triply periodic minimal surface gyroid structure as effective metal hydride hydrogen storage reactor: Experimental study. *Therm Sci Eng Progress* 42:101903. <https://doi.org/10.1016/j.tsep.2023.101903>
34. Li P, Yang F, Bian Y, Zhang S, Wang L (2023) Designable mechanical properties of modified body-centered cubic lattice materials. *Compos Struct* 317:117060. <https://doi.org/10.1016/j.compstruct.2023.117060>
35. Li X, Yu X, Chua JW, Lee HP, Ding J, Zhai W (2021) Microlattice metamaterials with simultaneous superior acoustic and mechanical energy absorption. *Small* 17:2100336. <https://doi.org/10.1002/smll.202100336>
36. Liang Y, Zhou W, Liu Y, Li Z, Yang Y, Xi H, Wu Z (2021) Energy absorption and deformation behavior of 3D Printed triply periodic minimal surface stainless steel cellular structures under compression. *Steel Res Int* 92:2000411. <https://doi.org/10.1002/srin.202000411>
37. Liu Y, Gall K, Dunn ML, McCluskey P (2004) Thermomechanics of shape memory polymer nanocomposites. *Mech Mater Active Mater* 36:929–940. <https://doi.org/10.1016/j.mechmat.2003.08.012>
38. Lu B, Weng Y, Li M, Qian Y, Leong KF, Tan MJ, Qian S (2019) A systematical review of 3D printable cementitious materials. *Constr Build Mater* 207:477–490. <https://doi.org/10.1016/j.conbuildmat.2019.02.144>
39. Ma S, Song K, Lan J, Ma L (2020) Biological and mechanical property analysis for designed heterogeneous porous scaffolds based on the refined TPMS. *J Mech Behav Biomed Mater* 107:103727. <https://doi.org/10.1016/j.jmbbm.2020.103727>
40. Maconachie T, Leary M, Tran P, Harris J, Liu Q, Lu G, Ruan D, Faruque O, Brandt M (2022) The effect of topology on the quasi-static and dynamic behavior of SLM AlSi10Mg lattice structures. *Int J Adv Manuf Technol* 118:4085–4104. <https://doi.org/10.1007/s00170-021-08203-y>
41. Martin O, Avérous L (2001) Poly(lactic acid): plasticization and properties of biodegradable multiphase systems. *Polymer* 42:6209–6219. [https://doi.org/10.1016/S0032-3861\(01\)00086-6](https://doi.org/10.1016/S0032-3861(01)00086-6)
42. Mehrpouya M, Edelijn T, Ibrahim M, Mohebshahedin A, Gisario A, Barletta M (2022) Functional behavior and energy absorption characteristics of additively manufactured smart sandwich structures. *Adv Eng Mater* 24:2200677. <https://doi.org/10.1002/adem.202200677>
43. Moerman KM (2018) GIBBON: The geometry and image-based bioengineering add-on. *J Open Source Softw* 3:506. <https://doi.org/10.21105/joss.00506>
44. Mohr R, Kratz K, Weigel T, Lucka-Gabor M, Moneke M, Lendlein A (2006) Initiation of shape-memory effect by inductive heating of magnetic nanoparticles in thermoplastic polymers. *Proc Natl Acad Sci* 103:3540–3545. <https://doi.org/10.1073/pnas.0600079103>
45. Mohsenizadeh M, Gasbarri F, Munther M, Beheshti A, Davami K (2018) Additively-manufactured lightweight Metamaterials for energy absorption. *Mater Des* 139:521–530. <https://doi.org/10.1016/j.matdes.2017.11.037>
46. Momeni F, Mehdi Hassani MS, Liu X, Ni J (2017) A review of 4D printing. *Mater Des* 122:42–79. <https://doi.org/10.1016/j.matdes.2017.02.068>
47. Montgomery SM, Wu S, Kuang X, Armstrong CD, Zemelka C, Ze Q, Zhang R, Zhao R, Qi HJ (2021) Magneto-mechanical metamaterials with widely tunable mechanical properties and acoustic band gaps. *Adv Func Mater* 31:2005319. <https://doi.org/10.1002/adfm.202005319>
48. Mukhopadhyay T, Adhikari S (2017) Stochastic mechanics of metamaterials. *Compos Struct* 162:85–97. <https://doi.org/10.1016/j.compstruct.2016.11.080>
49. Novak N, Al-Ketan O, Krstulović-Opara L, Rowshan R, Abu Al-Rub RK, Vesenjak M, Ren Z (2021) Quasi-static and dynamic compressive behavior of sheet TPMS cellular structures. *Compos Struct* 266:113801. <https://doi.org/10.1016/j.compstruct.2021.113801>
50. Obadimu SO, Kourousis KI (2021) Compressive behavior of additively manufactured lattice structures: A review. *Aerospace* 8:207. <https://doi.org/10.3390/aerospace8080207>
51. Ormiston S, Srinivas Sundarram S (2024) Fiberglass-reinforced triply periodic minimal surfaces (TPMS) lattice structures for energy absorption applications. *Polym Compos* 45:523–534. <https://doi.org/10.1002/pc.27795>
52. Ozdemir Z, Hernandez-Nava E, Tyas A, Warren JA, Fay SD, Goodall R, Todd I, Askes H (2016) Energy absorption in lattice structures in dynamics: Experiments. *Int J Impact Eng* 89:49–61. <https://doi.org/10.1016/j.ijimpeng.2015.10.007>
53. Pandzic A, Hodzic D (2021) Mechanical properties comparison of PLA, tough PLA and PC 3D printed materials with infill structure – Influence of infill pattern on tensile mechanical properties. *IOP Conf Ser: Mater Sci Eng* 1208:012019. <https://doi.org/10.1088/1757-899X/1208/1/012019>
54. Park K-M, Min K-S, Roh Y-S (2022) Design optimization of lattice structures under compression: Study of unit cell types and cell arrangements. *Materials* 15:97. <https://doi.org/10.3390/ma15010097>
55. Pei E (2014) 4D Printing: dawn of an emerging technology cycle. *Assem Autom* 34:310–314. <https://doi.org/10.1108/AA-07-2014-062>
56. Peng Y, Unluer C (2023) Development of alternative cementitious binders for 3D printing applications: A critical review of progress, advantages and challenges. *Compos B Eng* 252:110492. <https://doi.org/10.1016/j.compositesb.2022.110492>
57. Ravichander BB, Jagdale SH, Kumar G (2022) Surface morphology, compressive behavior, and energy absorption of graded triply periodic minimal surface 316L steel cellular structures fabricated by laser powder bed fusion. *Materials* 15:8294. <https://doi.org/10.3390/ma15238294>
58. Rismalia M, Hidajat SC, Permana IGR, Hadisujoto B, Muslimin M, Triawan F (2019) Infill pattern and density effects on the tensile properties of 3D printed PLA material. *J Phys: Conf Ser* 1402:044041. <https://doi.org/10.1088/1742-6596/1402/4/044041>
59. Sadeghi F, Baniassadi M, Shahidi A, Baghani M (2023) TPMS metamaterial structures based on shape memory polymers: Mechanical, thermal and thermomechanical assessment. *J Market Res* 23:3726–3743. <https://doi.org/10.1016/j.jmrt.2023.02.014>

60. Sahoo NG, Jung YC, Cho JW (2007) Electroactive Shape memory effect of polyurethane composites filled with carbon nanotubes and conducting polymer. *Mater Manuf Process* 22:419–423. <https://doi.org/10.1080/10426910701232857>
61. Sahu SK, Badgayan ND, Samanta S, Rama Sreekanth PS (2021) Evaluation of cell parameter variation on energy absorption characteristic of thermoplastic honeycomb sandwich structure. *Arab J Sci Eng* 46:12487–12507. <https://doi.org/10.1007/s13369-021-05987-9>
62. Saleh M, Anwar S, Al-Ahmari AM, Alfaiy A (2022) Compression performance and failure analysis of 3D-printed carbon fiber/PLA composite TPMS lattice structures. *Polymers* 14:4595. <https://doi.org/10.3390/polym14214595>
63. Schaedler TA, Jacobsen AJ, Torrents A, Sorensen AE, Lian J, Greer JR, Valdevit L, Carter WB (2011) Ultralight metallic Microlattices. *Science* 334:962–965. <https://doi.org/10.1126/science.1211649>
64. Shadrivov IV, Kozyrev AB, van der Weide D, Kivshar YS (2008) Nonlinear magnetic metamaterials. *Opt Express* 16:20266–20271. <https://doi.org/10.1364/OE.16.020266>
65. Shevchenko V, Balabanov S, Sychov M, Karimova L (2023) Prediction of cellular structure mechanical properties with the geometry of triply periodic minimal surfaces (TPMS). *ACS Omega* 8:26895–26905. <https://doi.org/10.1021/acsomega.3c01631>
66. Soyarslan C, Bargmann S, Pradas M, Weissmüller J (2018) 3D stochastic bicontinuous microstructures: Generation, topology and elasticity. *Acta Mater* 149:326–340. <https://doi.org/10.1016/j.actamat.2018.01.005>
67. Spoerk M, Gonzalez-Gutierrez J, Sapkota J, Schuschnigg S, Holzer C (2018) Effect of the printing bed temperature on the adhesion of parts produced by fused filament fabrication. *Plast Rubber Compos* 47:17–24. <https://doi.org/10.1080/14658011.2017.1399531>
68. Sun L, Huang WM, Ding Z, Zhao Y, Wang CC, Purnawali H, Tang C (2012) Stimulus-responsive shape memory materials: A review. *Mater Des* 33:577–640. <https://doi.org/10.1016/j.matdes.2011.04.065>
69. Sun ZP, Guo YB, Shim VPW (2021) Characterization and modeling of additively-manufactured polymeric hybrid lattice structures for energy absorption. *Int J Mech Sci* 191:106101. <https://doi.org/10.1016/j.ijmecsci.2020.106101>
70. Surjadi JU, Feng X, Fan R, Lin W, Li X, Lu Y (2021) Hollow medium-entropy alloy nanolattices with ultrahigh energy absorption and resilience. *NPG Asia Mater* 13:1–7. <https://doi.org/10.1038/s41427-021-00306-y>
71. Tancogne-Dejean T, Diamantopoulou M, Gorji MB, Bonatti C, Mohr D (2018) 3D plate-lattices: An emerging class of low-density metamaterial exhibiting optimal isotropic stiffness. *Adv Mater* 30:1803334. <https://doi.org/10.1002/adma.201803334>
72. Tancogne-Dejean T, Mohr D (2018) Stiffness and specific energy absorption of additively-manufactured metallic BCC metamaterials composed of tapered beams. *Int J Mech Sci* 141:101–116. <https://doi.org/10.1016/j.ijmecsci.2018.03.027>
73. Tang W, Zhou H, Zeng Y, Yan M, Jiang C, Yang P, Li Q, Li Z, Fu J, Huang Y, Zhao Y (2023) Analysis on the convective heat transfer process and performance evaluation of Triply Periodic Minimal Surface (TPMS) based on Diamond, Gyroid and Iwp. *Int J Heat Mass Transf* 201:123642. <https://doi.org/10.1016/j.ijheatmasstransfer.2022.123642>
74. Tibbitts S (2014) 4D printing: Multi-material shape change. *Archit Des* 84:116–121. <https://doi.org/10.1002/ad.1710>
75. Tobushi H, Hayashi S, Hoshio K, Miwa N (2006) Influence of strain-holding conditions on shape recovery and secondary-shape forming in polyurethane-shape memory polymer. *Smart Mater Struct* 15:1033. <https://doi.org/10.1088/0964-1726/15/4/016>
76. Torrents A, Schaedler TA, Jacobsen AJ, Carter WB, Valdevit L (2012) Characterization of nickel-based microlattice materials with structural hierarchy from the nanometer to the millimeter scale. *Acta Mater* 60:3511–3523. <https://doi.org/10.1016/j.actamat.2012.03.007>
77. Ushijima K, Cantwell WJ, Chen DH (2011) Estimation of the compressive and shear responses of three-dimensional micro-lattice structures. *Procedia Eng* 11th Int Conf Mech Behav Mater (ICM11) 10:2441–2446. <https://doi.org/10.1016/j.proeng.2011.04.402>
78. Vafaefar M, Moerman KM, Kavousi M, Vaughan TJ (2023) A morphological, topological and mechanical investigation of gyroid, spinodoid and dual-lattice algorithms as structural models of trabecular bone. *J Mech Behav Biomed Mater* 138:105584. <https://doi.org/10.1016/j.jmbbm.2022.105584>
79. Wojciechowski B, Xue Y, Rabbani A, Bolton JS, Sharma B (2023) Additively manufactured spinodoid sound absorbers. *Addit Manuf* 71:103608. <https://doi.org/10.1016/j.addma.2023.103608>
80. Wu X, Huang WM, Zhao Y, Ding Z, Tang C, Zhang J (2013) Mechanisms of the shape memory effect in polymeric materials. *Polymers* 5:1169–1202. <https://doi.org/10.3390/polym5041169>
81. Xiang Z, Zhang L, Yuan T, Li Y, Sun J (2018) Healability demonstrates enhanced shape-recovery of graphene-oxide-reinforced shape-memory polymeric films. *ACS Appl Mater Interfaces* 10:2897–2906. <https://doi.org/10.1021/acscami.7b14588>
82. Yan Q, Dong H, Su J, Han J, Song B, Wei Q, Shi Y (2018) A review of 3D printing technology for medical applications. *Engineering* 4:729–742. <https://doi.org/10.1016/j.eng.2018.07.021>
83. Yang C, Boorugu M, Dopp A, Ren J, Martin R, Han D, Choi W, Lee H (2019) 4D printing reconfigurable, deployable and mechanically tunable metamaterials. *Mater Horizon* 6:1244–1250. <https://doi.org/10.1039/C9MH00302A>
84. Yu S, Sun J, Bai J (2019) Investigation of functionally graded TPMS structures fabricated by additive manufacturing. *Mater Des* 182:108021. <https://doi.org/10.1016/j.matdes.2019.108021>
85. Yuan S, Chua CK, Zhou K (2019) 3D-printed mechanical metamaterials with high energy absorption. *Adv Mater Technol* 4:1800419. <https://doi.org/10.1002/admt.201800419>
86. Zhang L, Feih S, Daynes S, Chang S, Wang MY, Wei J, Lu WF (2018) Energy absorption characteristics of metallic triply periodic minimal surface sheet structures under compressive loading. *Addit Manuf* 23:505–515. <https://doi.org/10.1016/j.addma.2018.08.007>
87. Zhang W, Wu AS, Sun J, Quan Z, Gu B, Sun B, Cotton C, Heider D, Chou T-W (2017) Characterization of residual stress and deformation in additively manufactured ABS polymer and composite specimens. *Compos Sci Technol* 150:102–110. <https://doi.org/10.1016/j.compscitech.2017.07.017>
88. Zhang Y, Ren X, Han D, Cheng X, Jiang W, Zhang XG, Zhang XY, Xie YM (2022) Static and dynamic properties of a perforated metallic auxetic metamaterial with tunable stiffness and energy absorption. *Int J Impact Eng* 164:104193. <https://doi.org/10.1016/j.ijimpeng.2022.104193>
89. Zhao Q, Qi HJ, Xie T (2015) Recent progress in shape memory polymer: New behavior, enabling materials, and mechanistic understanding. *Progress Polym Sci Self-Heal Polym* 49–50:79–120. <https://doi.org/10.1016/j.progpolymsci.2015.04.001>
90. Zhou X, Li T, Wang J, Chen F, Zhou D, Liu Q, Li B, Cheng J, Zhou X, Zheng B (2018) Mechanochemical regulated origami with tough hydrogels by ion transfer printing. *ACS Appl Mater Interfaces* 10:9077–9084. <https://doi.org/10.1021/acscami.8b01610>
91. Zhou Y, Huang WM (2015) Shape memory effect in polymeric materials: Mechanisms and optimization. *Procedia IUTAM IUTAM Symp Mech Soft Act Mater* 12:83–92. <https://doi.org/10.1016/j.piutam.2014.12.010>

**Publisher's Note** Springer Nature remains neutral with regard to jurisdictional claims in published maps and institutional affiliations.